

A two-dimensional Dirac fermion microscope

¹*Peter Bøggild, ¹Jose M Caridad, ²Christoph Stampfer, ¹Gaetano Galogero, ¹Nick Papior, ¹Mads Brandbyge

*Corresponding author: peter.boggild@nanotech.dtu.dk

¹CNG, DTU Nanotech, Technical University of Denmark, DK-2800 Lyngby, Denmark

²JARA-FIT and 2nd Institute of Physics, RWTH Aachen University, 52074 Aachen, Germany

Abstract

The electron microscope has been a powerful, highly versatile workhorse in the fields of material and surface science, micro and nanotechnology, biology and geology, for nearly 80 years. The advent of two-dimensional materials opens new possibilities for realising an analogy to electron microscopy in the solid state. Here we provide a perspective view on how a two-dimensional (2D) Dirac fermion-based microscope can be realistically implemented and operated, using graphene as a vacuum chamber for ballistic electrons. We use semiclassical simulations to propose concrete architectures and design rules of 2D electron guns, deflectors, tunable lenses and various detectors. The simulations show how simple objects can be imaged with well-controlled and collimated in-plane beams consisting of relativistic charge carriers. Finally, we discuss the potential of such microscopes for investigating edges, terminations and defects, as well as interfaces, including external nanoscale structures such as adsorbed molecules, nanoparticles or quantum dots.

Graphene has proven to be an ideal host for spectacular mesoscopic effects, in particular after the introduction of hexagonal boron-nitride encapsulation¹⁻³ and efficient cleaning methods⁴⁻⁷, which reduces scattering rates towards the theoretical limits as mainly defined by electron-phonon^{2,5,8,9} and electron-electron^{10,11} interactions. At low temperatures, encapsulated graphene with mean free paths of up to 28 μm has been reported¹², while the phase coherence length of several micrometers can be reached^{13,14}.

Efforts have mainly been devoted to explore the Dirac fermion counterpart of conventional mesoscopic phenomena, occurring in finite effective mass electronic systems at cryogenic temperatures: integer^{9,15} and fractional¹⁶ quantum Hall effect, weak localization^{17,18}, Fabry-Perot oscillations¹³, commensurability oscillations¹⁹⁻²¹, universal conductance fluctuations^{22,23}, Aharonov-Bohm oscillations^{24,25}, magnetic focusing^{13,26,27} and quantized conductance^{28,29}. Here several factors set graphene apart from conventional two-dimensional systems. First, the linear gapless dispersion of graphene³⁰ gives rise to qualitatively different behaviors, such as Klein tunneling^{31,32} through potential barriers and Berry phase^{9,15} in magnetic fields. Klein tunneling allows Dirac fermions to penetrate high and wide barriers with zero reflection, which makes scattering at energy barriers resemble the transmission of light across an interface with an effective refractive index that can be tuned to negative values. Simply put, a single pn-junction constitutes an electron lens capable of focusing a beam of electrons, which was predicted for Dirac fermions by Veselago in 1967³³, shown to apply to graphene by Katsnelson³¹ and Cheianov³², and observed experimentally by numerous groups^{6,13,27,34,35}. Second, in contrast to a two-dimensional electron gas (2DEG) at the buried interface of GaAs and GaAlAs semiconductor crystals, graphene can be considered an open 2DEG, exhibiting highly tunable properties that strongly depend on its environment, as observed in Moiré superlattices²⁰ for graphene on hexagonal boron nitride (hBN) and trigonal warping of the

energy bands in bilayer graphene³⁶. Third, momentum relaxation mean free paths may reach up to micrometer scale at room temperature^{2,3,12,14,37}, hinting that ballistic transport could lead to new opportunities for electronics^{38,39} and optoelectronics^{40,41}. It was recently shown that the electron-electron scattering length, ℓ_{ee} , at elevated (room) temperature can be significantly smaller than the elastic mean free path, ℓ_{mfp} , as well as typical device dimensions, W , for ultraclean samples. It has been pointed out that high temperature transport resembles viscous flow, and may be understood in terms of hydrodynamics, see for example Refs^{10,42}. Some microscopic manifestations of ballistic transport such as magnetic focusing²⁶ and negative differential resistance⁴³, however, have been shown to survive at room temperatures. In the following, however, we exclusively focus on cryogenic temperatures, where both electron-electron and electron-phonon scattering processes are strongly suppressed, and where an upper limit for the mean free path is yet to be determined. With the steadily improving graphene device quality and the numerous confirmations that graphene is capable of supporting transport in the mesoscopic regime ($\ell_{mfp} > L \gg \lambda_F, \lambda_\phi$)^{2,6,12,19,26,34,35,44,45}, we find that complex instruments that utilize relativistic charge carriers for practical purposes has become realistic.

An ordinary scanning electron microscope is an extreme, yet familiar application of ballistic electron transport, which since its early incarnations more than 50 years ago has been a cornerstone of micro- and nanotechnology, surface and material science, as well as many other branches within natural sciences. The electron microscope is based on four functions: emission, focusing, deflection and detection of a focused beam of ballistic electrons in a vacuum chamber, with the aim of analyzing the shape, structure and chemistry of crystals, surfaces and small objects. The operation and individual components of an electron microscope in fact possess a striking number of similarities with state-of-the-art Dirac electron optics devices^{6,19,26,34,46}, and we note that the essential components and functions needed to realise such an instrument have been demonstrated

experimentally. In particular, two essential electron optics components were very recently proposed; the absorptive pinhole collimator by Barnard et al⁴⁷ and the parabolic lens by Liu et al⁴⁸.

We examine here such an apparatus: a two-dimensional electron microscope, based on the combination of elementary electron-optics components in a graphene device, which we in the following refer to as a Dirac fermion microscope (DFM). In this hypothetical instrument, Dirac quasiparticles move in straight trajectories within two-dimensional graphene rather than within a three-dimensional vacuum chamber. Electron beams may be focused onto intrinsic features such as grain boundaries, edges and defects, interfaces, contacts, edge terminations, and extrinsic nanoscale structures such as adsorbed molecules, nanoparticles, quantum dots and plasmonic superstructures to study their properties through their interaction with the electron system. Semiclassical ballistic calculations are effective in describing the overall magnetotransport characteristics in the mesoscopic limit⁴⁹ and are used to compare concrete architectures and designs suited for different types of target objects and applications.

Results

Anatomy of the Dirac fermion microscope. It is instructive to revisit the conventional scanning electron microscope and its components, see Fig. 1a. In an electron gun, electrons are extracted from a metal by thermal or field emission, and collimated and accelerated by electrical fields and apertures. The electron beam is then focused into a small spot on the target surface by tunable electrostatic or magnetic lenses, which can be scanned across the surface by another set of magnetic or electrostatic deflectors. A detector located nearby captures either backscattered or secondary electrons returning from the irradiated surface, allowing an image to be generated.

In the following we consider how these four tasks may be carried out with a graphene device, using an arrangement such as illustrated in Fig 1b. The 2D vacuum chamber is provided by graphene

itself; at sufficiently low temperatures the mean free path can be at least several tens of micrometers^{2,12}. As the lithographic resolution offered by high-end electron beam lithography can be of order 0.01 μm , there are nearly four orders of magnitude difference between the dimensions of the components and the characteristic transport lengths, such as the Fermi wavelength, which is $\lambda_F \approx 35 \text{ nm}$ at a carrier density of $n = 10^{12} \text{ cm}^{-2}$, which are typical numbers for ballistic graphene devices. The two-dimensional analogy of an electron gun can be realized by combining the functionality of basic components such as ballistic point contacts, apertures⁴⁷, Veselago lenses^{32,34} and superlattice collimators^{50,51}. Focusing of Dirac fermions can be carried by pn-junctions, where the carrier density can be controlled by electrostatic gates independently in the p- and n-doped regions. For the deflection of the beam, a perpendicular magnetic field provides a highly predictable means of controlling electron motion, as demonstrated in magnetic focusing^{13,26,35,44,47,52} and snake states^{6,45}. Detection can be done by large catch-all electrodes, or by arrays of smaller electrodes to provide position or angular resolved measurements³⁴. Fig. 1c shows a trajectory density plot (arbitrary scale) in the proposed Dirac fermion microscope calculated by a semiclassical Monte Carlo simulator (see Methods). The trajectory density corresponds roughly to the current density, since the Dirac fermions have a constant velocity. The electron gun is here a point injection contact and a grounded aperture⁴⁷, and the lens is a symmetric, linear pn-junction.

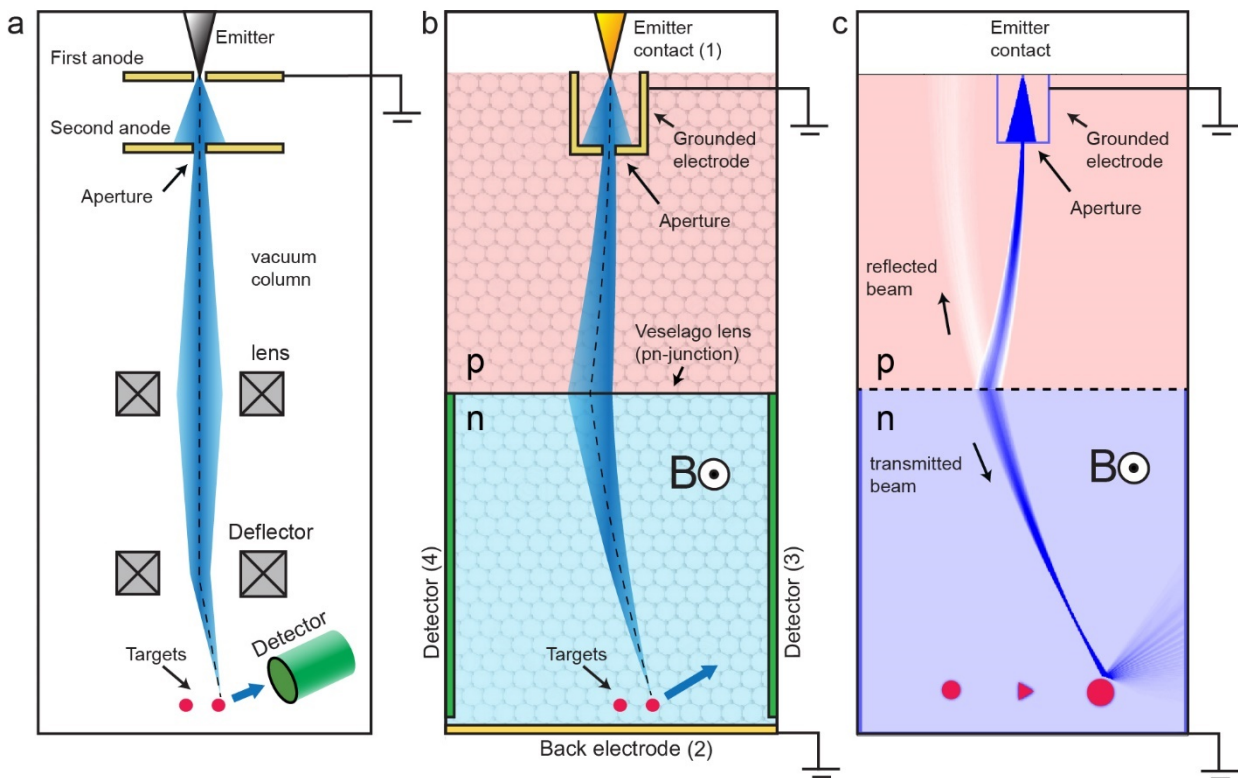


Figure 1. Conventional SEM versus Dirac fermion microscope. (a) Illustration of a scanning electron microscope with the electrons travelling in straight lines inside a vacuum column, from the emitter, through an aperture and a set of lenses that focus the electrons into a sharp beam at the surface. A deflection lens directs the electrons to a specific spot on the surface, from which they scatter back and are measured by a detector. (b) The 2D equivalent is a graphene device, where a narrow metal contact or an opening plays the role of the electron emitter, while a pn-junction provides guiding/lensing of the electron trajectories. A back electrode (2) collects electrons that are not intercepted by a target. Backscattered electrons are picked up by side-electrodes (3 and 4), allowing an image to be formed by measuring the transmission current. (c) Trajectory or current density from ballistic Monte Carlo simulation of a Dirac fermion microscope, where carriers are injected from a point-like emitter contact (1), collimated by an aperture and focused by a symmetric pn-junction electron lens. Part of the beam is reflected from the pn-junction as indicated. The

electron beam is seen to backscatter from one of the three targets, giving rise to a current flowing between electrodes 1 and 3, instead of 1 and 2.

Graphene as a two-dimensional vacuum chamber. The vacuum chamber must provide an unobscured path for the electron beam, with low presence of scatterers and with sidewalls of the microscope removed out of the beam path. Most graphene electron optics devices published in literature, such as Hall bar or van der Pauw geometries, have sidewalls within a distance of λ_{mfp} from the current pathways. In the ballistic limit, reflecting walls may add a non-trivial background to the conductance signal of interest, which may become more complex in coherent conditions (see e.g. Ref⁵³, Fig 4), analogous to reverberation and standing acoustic waves in a poorly dampened room. This may lead to a conductance background in the vein of weak localization, conductance fluctuations, Fabry-Perot oscillations and Aharonov-Bohm oscillations. If the confining potential has strong geometric symmetries, the conductance fluctuations can exhibit pronounced regular features. We suggest that a graphene vacuum chamber should be designed either with semi-infinite sidewalls, i.e. $W \gg \ell_{\text{mfp}}, \ell_{\phi}$ such that the electron momentum and phase are fully randomized before the carriers return, or by diffusive walls, i.e. with non-specular reflection to suppress unwanted ballistic and coherent reflections. Recently, electrically grounded electrodes were shown to act as walls that remove carriers from the vacuum chamber, and prevent them from returning to the main path of the beam⁴⁷.

Sidewalls are themselves relevant as objects of study with a DFM, given their importance for ballistic transport and devices depending thereof. Magnetic focusing of Dirac fermions has already been used to characterize the edge roughness and scattering properties of lithographically defined graphene edges^{46,47}. An intriguing possibility is to probe pristine microcleaved edges; these offer

near zero structural disorder with either armchair or zig-zag structure that have been predicted to exhibit distinctly different scattering properties⁵⁴.

Electron guns. The electron gun is the component, or collection of components, that together generate a collimated, intense beam of electrons. In graphene devices, electrons are directly injected by metal-graphene contacts^{6,12,35,52}, or by ballistic graphene contacts where the metal-graphene contact region is located outside the main device area^{34,46}. While both these contact types are suitable, they result in point-like injection, since the task of focusing an electron beam to achieve a narrow diameter at the target area is greatly simplified if the electrons are injected from a point-like source, in analogy with light and electron optics. In analogy with classical wave mechanics, a point contact will have a wide distribution of injection angles⁴⁷, with the special case of a rectangular, ballistic contact having a $\cos\theta$ distribution⁵⁵. While size effects such as conductance quantization^{28,29}, Fabry-Perot-like interferences and sidewall roughness in the electron emitter may alter the angular distributions, we consider here the mesoscopic limit, where coherence and diffraction effects do not mask the overall behavior⁵⁶. For electron optics as for any type of optics, apertures provide straightforward means of reducing the angular spread of the beam, which was recently demonstrated experimentally by Barnard et al.⁴⁷. The authors showed that a metal contact aperture connected to electrical ground can be used to obtain a significant reduction of the beam divergence in a graphene device, while at the same time removing stray electrons from the device.

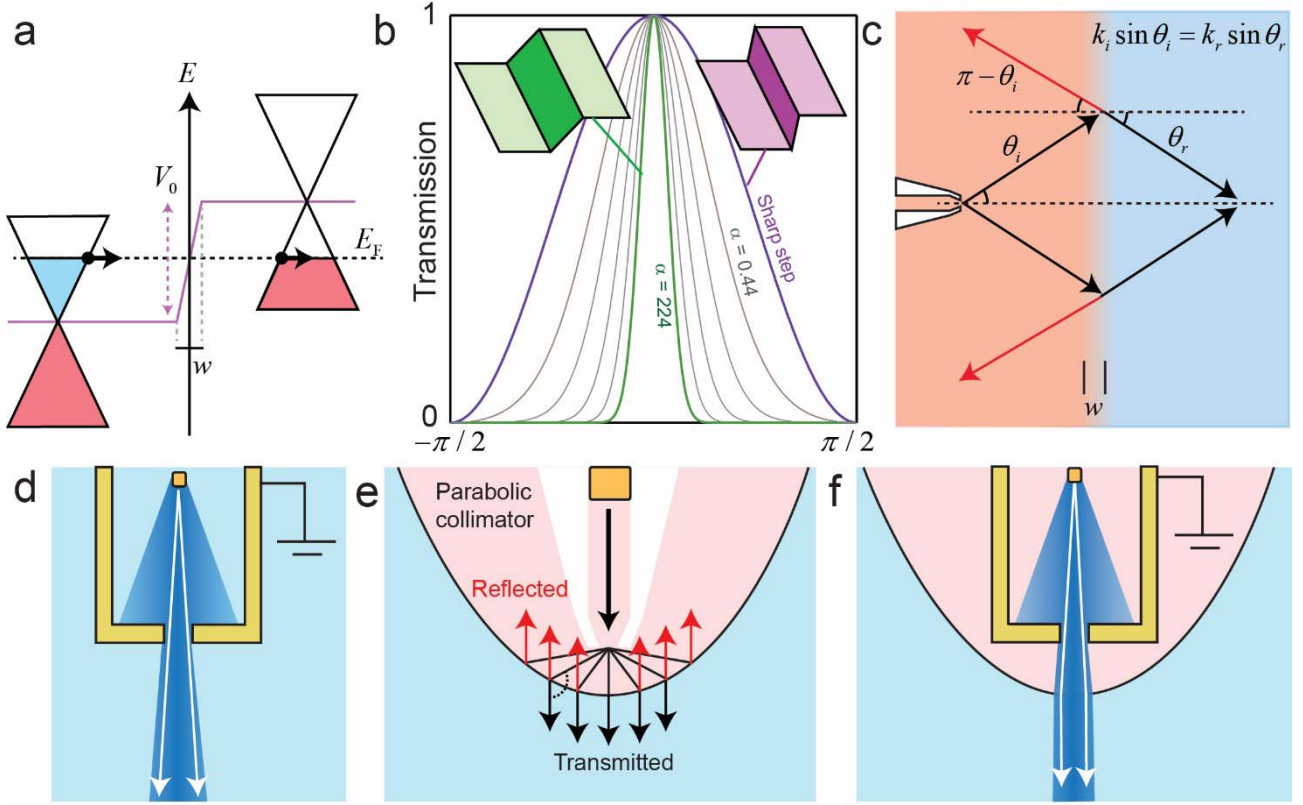


Figure 2. Electron gun and optics. (a) Illustration of two Dirac cones offset by a potential step of height V_0 . The width of the potential step is w . Carriers moving from the left (n-type) to the right (p-type) perpendicular to the step, but cannot be backscattered due to conservation of pseudospin. (b) The transmission through a potential step depends strongly on $\alpha = k_F w$, with large w exhibiting a larger chance of reflection at oblique angles. The analytical angular distributions⁵⁷ from sharp to soft ($w = 40$ nm at $n = 10^{12}$ cm⁻²) pn-junctions, with intermediate curves calculated by Cayssols interpolation curve⁵⁸ for $\alpha = 0.44 - 244$ are shown. (c) Electrons impinging on a pn-junction at an angle θ_i with respect to the normal, are transmitted/refracted according to Snell-Descartes law, or specularly reflected. (d) An aperture limiting the angular distribution. (e) A pn-junction lens with a parabolic shape and the point contact positioned in the focus, will co-align the transmitted trajectories. (f) A combination of an aperture and a parabolic lens produces an electron beam with a long focal length.

Electron lenses and focusing. Klein tunneling has been extensively described in literature, e.g. Refs³¹⁻³³ as well as comprehensively reviewed by Allain and Fuchs⁵⁷. Here we outline just a few particularly relevant features. Klein tunneling is the suppression of backscattering due to pseudospin conservation for an electron impinging on a potential step or barrier so that it will be transmitted with unity probability as illustrated in Fig 2a. While the transmission is unity for incident angle $\theta_i = 0$, the angular transmission function depends on the width w of the potential step compared to the electron wavelength, translating into an effective smoothness $\alpha = k_F w$ of the step. For a hard, symmetric potential step, $k_i = k_r$ and $\alpha < 1$, the angular distribution⁵⁷ is given by $T(\theta_i) = \cos^2 \theta_i$. For a carrier density of $n = 10^{12} \text{ cm}^{-2}$, which we use throughout the simulations, the Fermi wavelength is $\lambda_F = 2\pi(\pi n)^{-1/2} \approx 35 \text{ nm}$, while the effective smoothness α is unity for a width of $w = 5.6 \text{ nm}$. Analytical expressions for the optical properties of potential steps and barriers in the sharp and soft limits are known for a number of situations⁵⁷, and we use here Cayssols^{39,57} interpolation formula that connects the two regimes, see Fig. 2b. As illustrated in Fig. 2c, the incident and refracted angles, θ_i and θ_r , follow the Snell-Descartes law:

$$k_i \sin \theta_i = -k_r \sin \theta_r \quad (1)$$

where k_i and k_r are the Fermi wavenumbers corresponding to the carrier densities in the two regions, n_i and n_r , and the effective negative refractive index is given by $-(n_i / n_r)^{1/2}$. The transmission probability is unity for perpendicular incident angle, $\sin \theta_i = 0$, and the case of reflection gives $\theta_r = \pi - \theta_i$, as illustrated in Fig. 2c. While pn-junctions constitute electron lenses capable of focusing a beam of electrons in graphene, steep and smooth pn-junctions behave very differently and should serve different purposes in the 2D electron microscope, see Fig. 1a. The steep pn-junction provides high transmissivity with a broad angular acceptance window, and is well

suitable for electron lensing, where reflection is best kept at a minimum. A smooth pn-junction has a strong tendency to filter oblique angles, which can be used to collimate beams⁵¹ as well as for electron guides and mirrors⁵².

Such a pn-junction can be formed by electrostatic gating, such as the split bottom gates^{6,59} or top-gates³⁴, or by chemical gating, where metal islands deposited directly on top of the graphene provide the charge transfer necessary to induce potential steps or barriers⁶⁰. For electrostatic gates, the width of the pn-junction can be controlled by the thickness of the dielectric spacer between the graphene and the gate³⁴, which suggests that an architecture that supports both reflective/filtering and transmission/lensing components could be realized with two top and bottom dielectric layers of different thickness.

Until now, little has been done to explore the possibilities and properties of curved pn-junctions for electron optics, perhaps due to the fact that the linear pn-junction itself is perfectly capable of focusing a Dirac electron beam³³. In the language of optics, the linear Veselago lens suffers from significant aberration for non-zero magnetic fields, which makes it a less suitable starting point for a scanning beam microscope based on magnetic deflection. Inspired by parabolic mirrors that convert divergent rays from a source placed at the focus point into parallel rays, we employ the same principle to collimate and manipulate the electron beam as illustrated in Fig 2e. A symmetric, parabolic pn-junction with the point contact placed in the focal point constitutes a parabolic electron gun with perfect collimation of transmitted electrons $\theta_r = 0$ for all θ_i according to Eq. (1) as well as reflection of trajectories with $\theta_r = -\pi$. The parabolic pn-junction greatly reduces the angular spread, and increases the focal depth of the electron beam, ultimately offering a possibility of maintaining a parallel, focused beam across large scanning fields with much reduced aberration. Recent work by Richter and coworkers solves the real-space Greens function in a tight-binding

framework to analyse the detailed properties of the parabolic pn-junction. They predict that a parabolic pn-junction is capable of co-aligning a beam of Dirac fermions, and that such a beam can be deflected by a weak magnetic field without losing the collimation⁴⁸.

Deflection. A perpendicular magnetic field provides a means of deflecting the path of ballistic electrons in a way that is predictable and easy to control, as demonstrated for magnetic focusing in large number of experiments in both III-V and graphene mesoscopic systems^{44,46,47,49,52,54}. The cyclotron radius is given by $R_c = \hbar k_F e^{-1} B^{-1}$. It follows from $k_F = (\pi n)^{1/2}$ that the cyclotron radius scales with $n^{1/2}$, while the cyclotron motion changes direction by reversal of either B or carrier polarity, i.e. from n- to p-doped regions. In magnetic focusing, wide distributions of injected electrons lead to trajectories with pronounced caustics, which result in an oscillatory conductance with maxima at the point where the caustics intersect with the extraction point contact. In analogy with conventional optics, the width and shape of the caustic beam should indeed depend on the sidewalls, and could therefore be used to extract information of the sidewall roughness⁴⁷ and electrostatic potential near edges⁴⁶. Since only certain discrete reflection points are being probed at each geometrically resonant magnetic field, imaging of the edge as such cannot be carried out, unless an array of contacts³⁴ is used to provide spatial or angular resolution. While magnetic focusing is normally carried out at intermediate magnetic fields, $R_c \leq L$, where L represents the characteristic dimensions of the sample, we consider in this work exclusively the low magnetic field limit, i.e. $R_c \gg L$, where only slight bending of the electron beam is used to scan the focused beam spot across a feature; this situation closely mimics the image formation in a scanning electron microscope. An example of how this could be done is shown in Supplementary Figure 2.

Detectors and image formation. The simplest detector consists of a point contact. Imaging requires the extraction of the spatial distribution of some characteristic property, following an

interaction between the sample and the probe, which in this case is a beam of Dirac fermions. While it is tempting to use an array of electrodes to pick up spatial information, similar to the charge coupled device (CCD) sensor in a transmission electron microscope (TEM), we consider a simpler scenario here that bear some resemblance to the architecture of a scanning electron microscope (SEM), see Fig. 1. We find that two large catch-all contacts (left and right) are sufficient to generate images that discern between sizes, shapes and orientations of obstacles with sizes comparable to or above the beam diameter. The back-plane is an absorptive electrode, which can be used to catch the carriers similar to a Faraday cup, allowing the beam current to be measured as in a conventional SEM. The images are constructed from the transmission between source and detector/drain electrodes as a function of magnetic field, which is the number of electrons arriving at the detector electrode, divided by the number of electrons emitted by the source. The transmission includes the ballistic contact resistance of the electron gun, which depends greatly on the exact gun configuration. However, as in a conventional microscope, only the relative intensity variations matter, hence contrast and brightness adjustments are needed to achieve a useful image. Transmission values and trajectory (current) densities are therefore arbitrary scale.

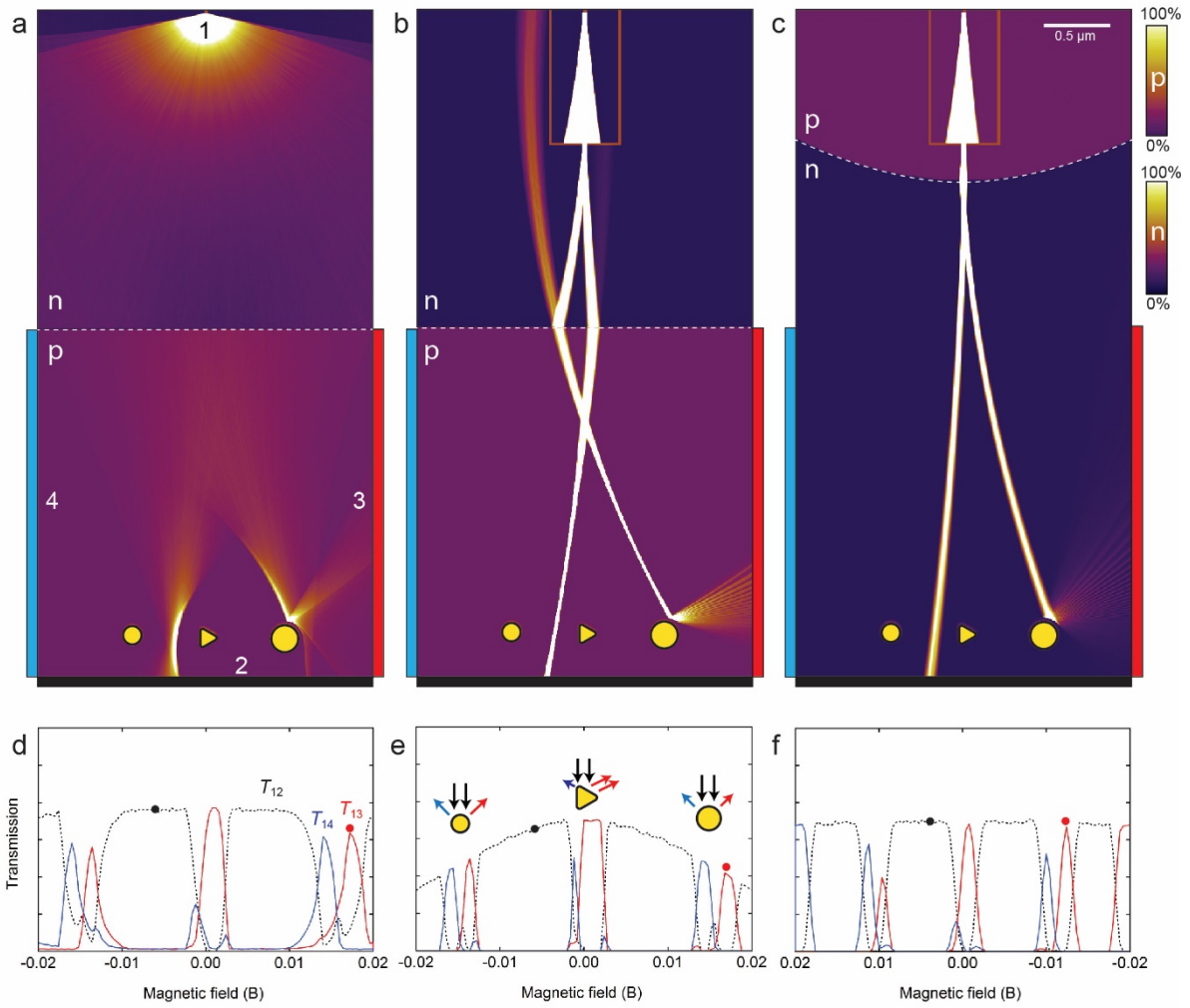


Figure 3. Imaging with Dirac fermions. Current density maps of three DFM microscope configurations, (a) Veselago, (b) Pinhole/Veselago and (c) Pinhole/Parabolic lens. In each case, the current density for two different magnetic fields are overlaid, indicated with black and red dots in panels below. Color scales ranging from 0% (zero current density) to 100% (high current density) are used to visualize zones with different carrier polarity p and n. (d-f) The dashed black curves show the transmissions from electrode 1 to the back electrode 2, while red and blue curves represent carriers exiting at the right (3) and left (4) electrodes, respectively, as also indicated in panel a. The transmission images from the three target objects are distinctly different, with the spherical objects leading to relatively symmetric peaks, and the triangular object giving rise to a sharp transmission peak from reflection at the left corner of the triangle, and a broader peak or plateau corresponding to

reflection from the flat, right-hand side of the triangle. Of the three selected configurations, the configuration (a) exhibits the largest aberration and image distortions, configuration (b) the sharpest features due to highly focused beam, while (c) maintains a constant transmission current across the image field. The three configurations are analysed with respect to beam profile, angular distribution and linearity with respect to the magnetic field in Supplementary Note 1 and Supplementary Fig. 1. The imaging is showing during operation in Supplementary Movie 1.

Scanning DFM microscopy with single emitter. We have performed extensive Monte Carlo simulations to compare different microscope configurations, and have analysed the behavior of the microscope components and simulated the image formation in scanning DFM (see Methods for details). The lens components we combine in order to obtain control of the shape, angle, divergence and position of the beam, are the grounded aperture (absorptive pinhole collimator)⁴⁷, the parabolic pn-junction for co-aligning the electron trajectories and the linear Veselago lens³² for refocusing a divergent beam. The beam profile and angular distributions, as well as linearity of beam position with respect to magnetic field are shown in Supplementary Fig. 1.

In Fig. 3, we compare simulated images of the three microscope configurations. The target consists of three antidots; two circular shapes of different diameter and a triangular shape. Fig. 3a-3c show the overlaid trajectory density as well as the transmission between source 1 and either drain 2 (the backplane electrode) or drains 3 or 4 (detector electrodes), with two magnetic fields for each microscope configuration. Due to the constant carrier velocity, $v_F \approx 10^6$ m/s, the trajectory density is directly proportional to the semiclassical (non-coherent) current density. Fig. 3d-3e show the transmission T_{12} , T_{13} and T_{14} as a function of the magnetic B-field, between injection electrode 1 and the three drain electrodes 2, 3 and 4, respectively. As the magnetic field sweeps the electron

beam across the target, shape-specific features appear in the magneto-transmissions T_{13} and T_{14} , which in the following will be referred to as transmission images. The spherical scatterers generate two peaks of equal height and shape, spaced roughly by the projected width of the circular potential. The triangle gives rise to a narrow peak from the leftmost corner, and a broader peak or plateau corresponding to the flat, right-hand side. While these features are recognizable in all three configurations, they are more sharply defined for Fig. 3b compared to Fig. 3a, which is distorted by the broader angular distribution of incoming electrons and Fig. 3c which is characterized by a long focal length, but also a wider beam diameter. The relative transmission for Fig. 3b and to a lesser extent Fig. 3c is decreasing with magnetic field, as large field magnitudes cause the electron trajectories to intersect the pn-junction at higher angles, thereby reducing the transmission probability. The Supplementary Note 4 shows the imaging process for two different aperture sizes, with only minor difference in image quality.

In general terms, a symmetric Veselago lens creates a mirror image of the point-like source, which is distorted by varying the carrier density on one side³², or by a finite magnetic field. Due to the pronounced caustics resulting from Dirac fermions passing a linear Veselago lens, it is still possible to generate an image with a high spatial resolution. Moreover, the caustic beam spot position is nearly perfectly linear in magnetic field, see Supplementary Fig. 1. This situation can be augmented by introducing other lens components. An aperture will limit the angular spread by blocking most of the diverging beam, while a parabolic lens reduces the angular spread by co-aligning the beams. The combination can give a beam with exceedingly low angular spread, and therefore very long focal depth.

Another strategy to provide spatial image resolution is to use arrays of collector electrodes. This approach could be useful for imaging by magnetic focusing, where the reflection point can be swept across an edge, while the collector array picks up the backscattered electrons. An example of such a

magnetic focusing-based imaging of edge roughness using five electrodes is shown in Supplementary Fig. 2, and Supplementary Movie 5.

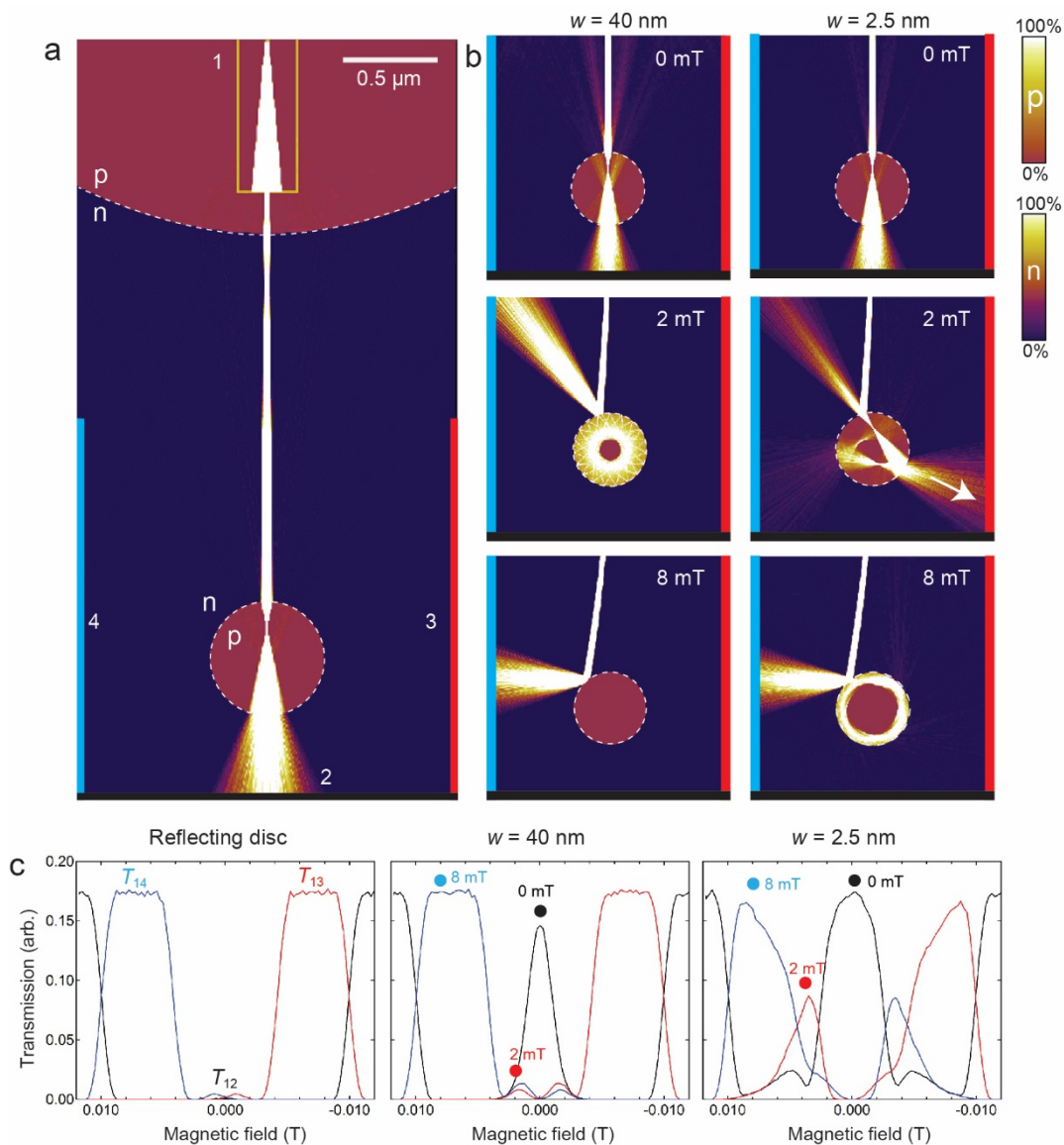


Figure 4. Imaging of Veselago dots. (a) Focused electron beam directed towards a circular pn-junction, a so-called Veselago Dot (VD), using the DFM configuration in Fig. 3c. The transmission into the VD depends on the angle of the incoming beam with respect to the junction wall. At zero incidence angle (along the center line), the beam is nearly fully transmitted through the dot, before hitting the back electrode (2, black). (b) shows the current density for two different pn-junction

width, $w = 2.5$ nm (close to hard-wall limit) and $w = 40$ nm. hBN layers thickness is typically in the range 10-100 nm^{34,47}. Color scales ranging from 0% (zero current density) to 100% (high current density) are used to visualize zones (p,n) with different carrier polarity. (c) The calculated transmission coefficients, T_{12} (black curve), T_{13} (red curve) and T_{14} (blue curve), for the three drain electrodes as a function of magnetic field, plotted for two VD with $w = 40$ nm and $w = 2.5$ nm, as well as a reflecting disc. The magnetic field values of 0, 2 mT and 8 mT are marked as black, red and blue dots. At 2 mT, the current jet emitted towards electrode 3 for the $w = 2.5$ nm VD is shown as a large peak (red curve) in the transmission image. At $w = 40$ nm the jet is much weaker.

Imaging of Veselago dots. A different type of scattering potential is the closed pn-junction, which we here term a Veselago dot (VD). Gutierrez et al⁶¹ found that few-nanometer graphene pn-junctions formed in continuous graphene on copper due to local variations in surface interactions and surface potential showed the signatures of distinct quantum states corresponding to periodic polygonal trajectories inside the potential. Caridad et al⁶⁰ formed arrays of VD by depositing metal dots directly on graphene to locally pin the electrostatic potential, leading to sharp, circular pn-junctions by tuning of the back gate to the opposite polarity. The VD-like behavior was corroborated by measurement of Mie-like scattering of the electron waves on tilted arrays of VD with respect to the current direction. VD are lens-like potentials that can reflect, trap and reemit electrons depending on their incident angle, width and height of energy barrier, and serves a double role as interesting objects of study, as well as potentially useful and simple electron optics components with naturally hard pn-junctions and no need for a gate dielectric.

Fig. 4 shows simulated current density plots for three different spherical potentials: pn-junctions with $w = 2.5$ nm and $w = 40$ nm, as well as a fully reflective disc-shaped potential. At certain

magnetic fields, the focused beam leads to pronounced, internal scattering patterns and narrow emission jets at the reflection points, which can be thought of as classical counterparts of jets in optical cavities⁶². For glancing incident angles, the $w = 40$ nm VD reflects all trajectories, while for the $w = 2.5$ nm VD, high-order polynomial closed trajectories appear inside the boundary. The caustic emission jets lead to local transmission maxima (red dots) at the electrode opposing the main reflection direction (blue dots). These distinct signatures of the scattering profile depends strongly on the width w , shape and height of VD, and can be used to analyse the properties of pn-junctions down to very small widths⁶⁰. Supplementary Movie 2 shows the development of current density corresponding to Fig. 4.

Scanning DFM microscopy with multiple emitters and coaligned beam. For a coherent electron system, such as high quality graphene at cryogenic temperatures^{22,63,64}, classical periodic orbits are directly related to bound quantum states, and can be used to predict the energy level spectrum⁶⁵ and transport properties^{66,67}. For an open or semi-open quantum billiard⁶³ - a constant confinement potential with hard or soft sidewalls - electrons are injected via point contacts at the edge of the potential, which makes stable periodic orbits classically inaccessible without scattering⁶⁷. The injection point contact itself will scatter any polygonal orbit on the first roundtrip. For the VD, the situation is entirely different; the semitransparent pn-junction will indeed allow carriers to be injected directly into a periodic orbit, as shown in Fig. 4.

In Fig. 5a we introduce a microscope configuration that mimics the nearly parallel electron beam of a conventional SEM, allowing the beam to pass through the target area without changing focus or angle. The aperture is placed at the focus of the parabolic lens, and the single emitter is replaced by an array of N point emitters. The beam will be aligned parallel to the center axis by passage across the parabolic pn-junction, and the slight divergent beam can optionally be refocused using a symmetric Veselago lens, as in Figure 3a. The result is a narrow beam that can be moved in coarse

steps between N positions, corresponding to the N emitter electrodes. The beam position can be further fine-tuned by the magnetic field, leading to seamless coverage of the image plane, as indicated with the dashed line. Full-range scanning requires stitching of the regions defined by the selected emitter electrodes by fine-tuning of the magnetic field. Together, the emitter array, the aperture and the parabolic lens constitute a composite electron optics electron gun with a low aberration, near-parallel beam and a large scan range.

Fig. 5b depicts the transmission image profile of circular and triangular reflective targets similar to those imaged in Fig. 3, with the T_{12} , T_{13} and T_{14} curves shown both before (dashed lines) and after (full lines) compensation for the unavoidable current decrease at large offsets, where the collimated beam intersects the parabolic lens at oblique angles.

The lower panel shows the position of the beam at the electrode depending on emitter electrode and magnetic field between ca. -1 mT and 1 mT, with the white marker indicating the sequence of emitter position (1-9) and B-field used to achieve a continuous scan. This strategy is similar to the separate deflector systems for coarse and fine alignment in an electron beam lithography system, where small regions are stitched together into large continuous regions, to avoid large beam deflections and image distortions. After correction, the transmission image of the circular potential is symmetric, while the image of the triangular potential shows a pronounced flat part (red curve), corresponding to the flat part of the triangle, facing right.

Fig. 5c shows a wide-angle distribution of trajectories being co-aligned by a parabolic lens, and directed at a circular pn-junction with $w = 2.5$ nm. A clear pattern of caustics is visible, which agrees exactly with those predicted by differential geometry (see Supplementary Note 2 and Supplementary Fig. 3). In Fig. 5d and 5e, a focused beam is directed at the injection points for the

triangular and square polygonal closed orbits⁶¹, leading to strong caustic resonances and collimated emission jets at the corners.

Fig. 6 shows transmission images of 200 nm wide VD structures, with effective width of the pn-junction ranging from $w = 2.5$ nm to $w = 40$ nm, see Fig 2b. Fig 6a shows current density for four selected magnetic fields, indicated with arrows on the transmission image (Fig. 5b). While the forward transmission peak in the coefficient T_{12} (black curve) due to Mie-like scattering^{60,68} is relatively insensitive to w , T_{13} (red curve) and T_{14} (blue curve) show distinct features related to the intensity of the caustic jets, with a clear dependence on w . This shows that the spatial mapping can indeed provide detailed information of the nanoscopic properties of the scattering potentials.

In Supplementary Note 3 we discuss how a DFM may be fabricated using van der Waals assembly³⁷. In Supplementary Fig. 5 we show that the transmission images are robust towards increasing the aperture size, which can be advantageous to reduce diffraction effects for low carrier densities, large Fermi wavelength and narrow apertures⁴⁷. Supplementary Movie 3 illustrates current density variations during imaging of two different VDs and a reflecting disc, and Supplementary Movie 4 shows imaging and caustic jets of a large VD using multiple emitter Dirac fermion microscopy.

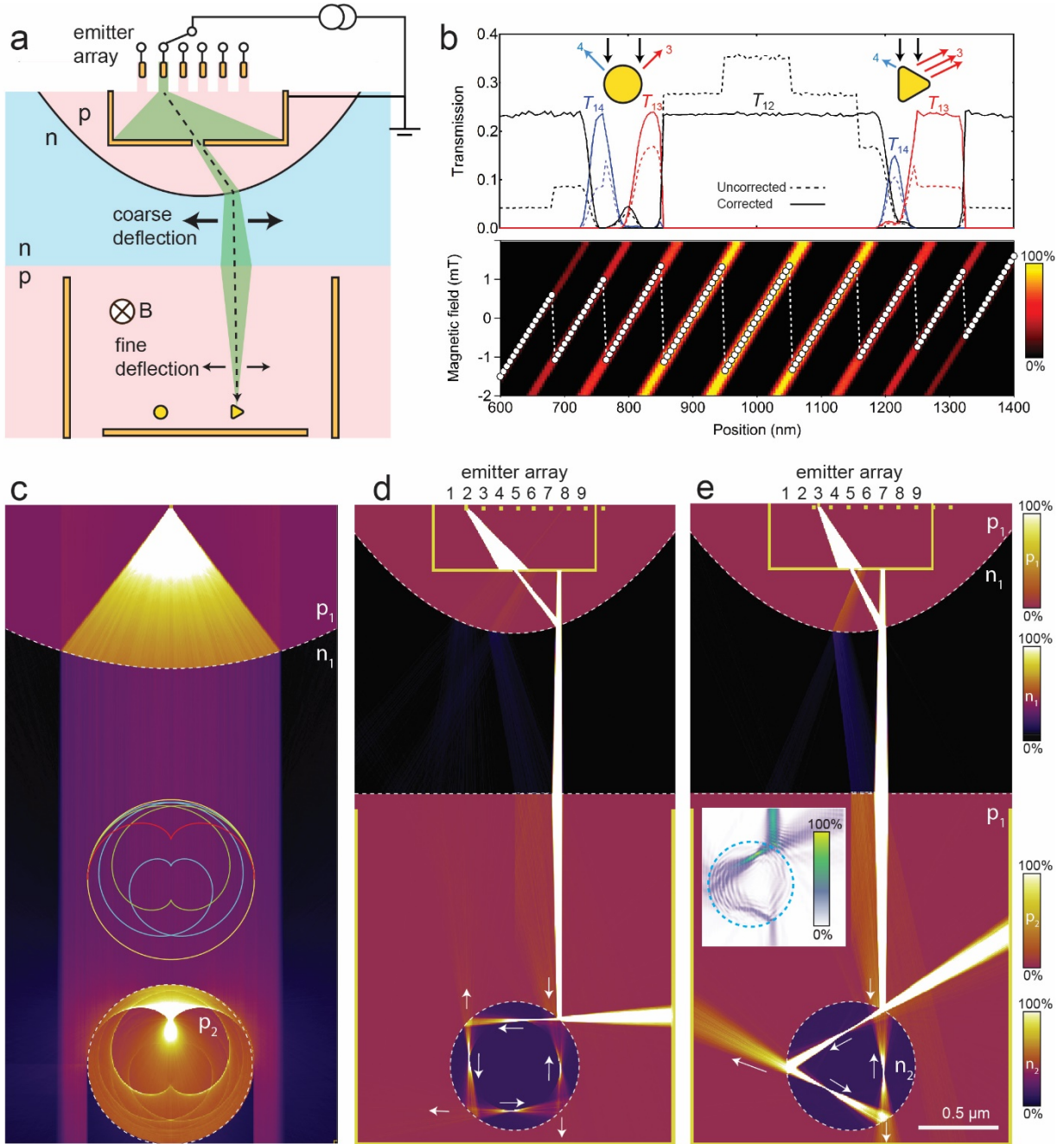


Figure 5. Dirac fermion microscope with multiple emitters and coaligned beam. (a) Illustration of the coaligned scanning Dirac fermion microscope, where an array of emission electrodes and a parabolic pn-junction allows for lateral displacement of a vertically aligned beam of electrons. A small magnetic field provides fine adjustment of the beam position. (b) Transmission from emitter to electrode 2 (bottom), electrode 3 (right) and electrode 4 (left) before (dashed) and after (full

lines) correction for emission current variations of the 9 emitters. The lower panel shows the switching between emitter electrode (9,8,7,...,1) and magnetic field (y-axis) needed to produce a continuous coaligned scan. (c) Parallel beam of electrons scattering on a circular pn-junction ($w=2.5$ nm), producing the well-known caustic pattern of trajectories in a circular potential (see Supplementary Note 2). (d-e) Injection of current directly into square and triangular closed orbits. The carriers are transmitted out at the three corners, producing well-collimated jets. Color scales ranging from 0% (zero current density) to 100% (high current density) are used to visualize zones (p_1, n_1, p_2, n_2) with different carrier polarity in panels c-e. The inset in panel (e) shows the bond current results from an atomistic transport calculation of a graphene VD with a similar ratio between diameter and λ_F as used in the semiclassical simulation, resulting in a current density resembling the triangular closed orbit and a current jet emission pattern qualitatively in agreement with the semiclassical simulation. The quantum transport calculations are detailed in Supplementary Note 3.

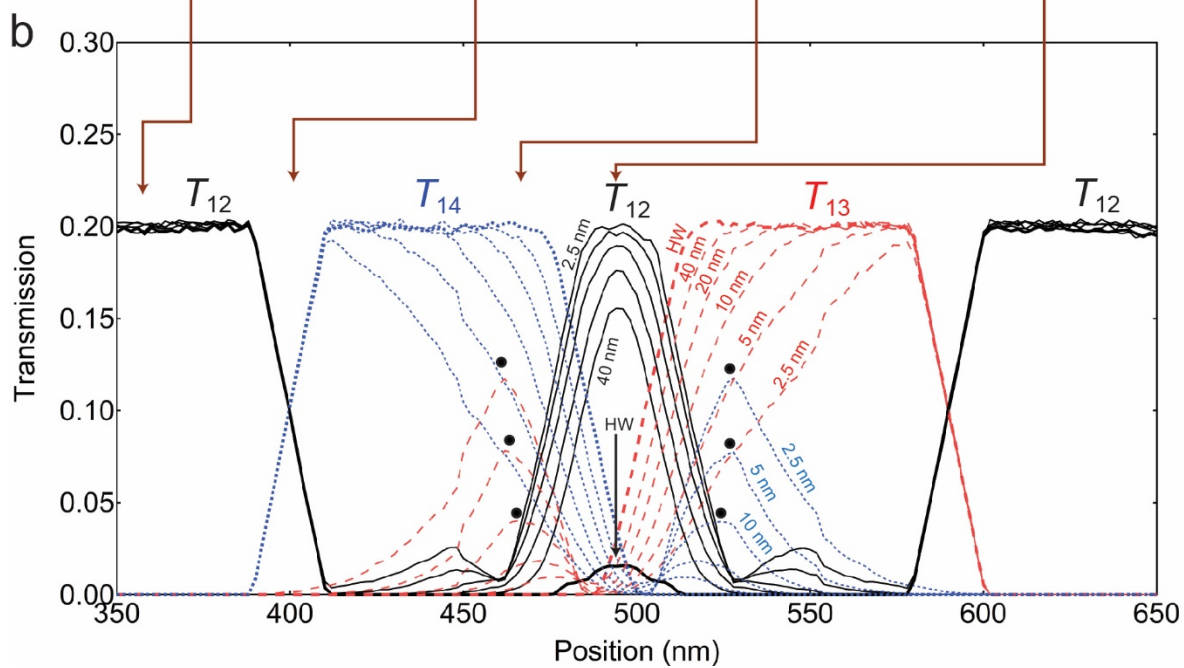
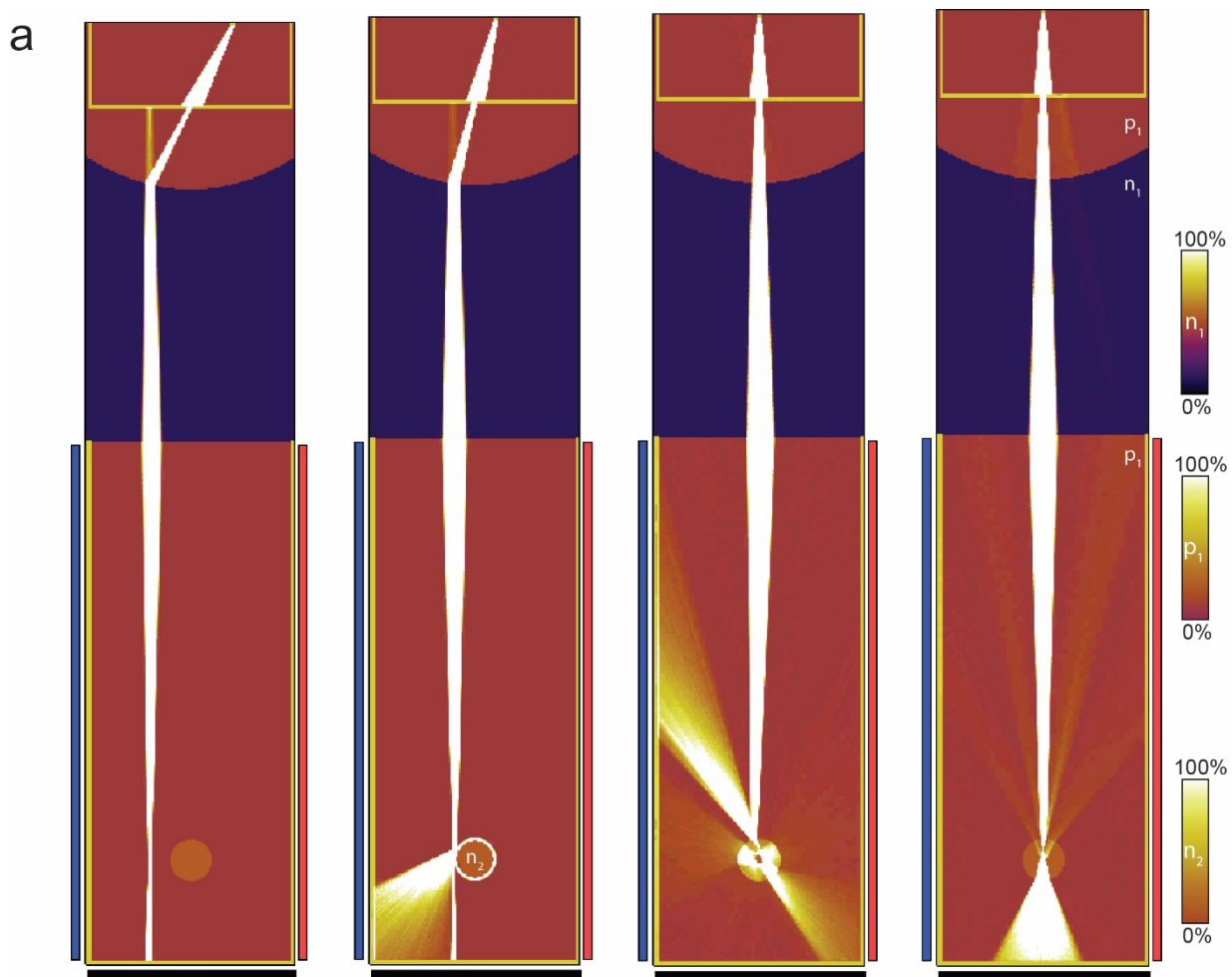


Figure 6. Imaging of Veselago dots with different smoothness. (a) Current density plots in a $1 \times 4.5 \mu\text{m}$ DFM with 200 nm diameter VD targets for 4 different magnetic fields, indicated with arrows in the panel b below. The width of the pn-junctions is $w = 10 \text{ nm}$. (b) Development of transmission image for VDs with different width ($w = 2.5, 5, 10, 20$ and 40 nm) as well as hard-walled, reflective potential (HW), for the four magnetic fields simulated in (a). The dotted, blue curves correspond to the transmission T_{14} , for electrode 4, while the dashed, red curves represent the transmission T_{13} , for electrode 3. The black, full curves show the transmission T_{12} between electrode 1 and the backplane electrode 2. While the zero-incident angle peak (at 500 nm) does not change significantly with w , the transmission side-bands caused by caustic jets, at 400-500 nm and 500-600 nm, changes dramatically from $w = 2.5 \text{ nm}$ to $w = 40 \text{ nm}$ (marked with black dots).

Discussion

We have described a class of devices that through control and scanning of a beam of relativistic carriers allows a form of in-plane scanning microscopy in two dimensions, and show examples of how imaging of different types of objects could be carried out, and how different beam profiles and behavior can result from the interplay of the electron optics components. Obviously, these can be combined in far more ways than shown here.

There are several issues that should be addressed. First, the question of whether the graphene can provide the disorder free vacuum chamber at low temperatures. As of now, the highest reported elastic mean free path in graphene is $28 \mu\text{m}^{12}$, but so far no fundamental upper limit has been reported. It appears that the cleanliness of the interfaces, quality of the materials and strain inhomogeneities are the limiting factors, as the intrinsic electron-phonon scattering processes freeze

out at cryogenic temperatures. For III-V heterostructures, mean free paths in excess of 100 μm have been reported⁶⁹. The mean free paths in cryogenic graphene could be even longer.

One potential problem with narrow beams that are guided across long distances by small magnetic fields, is that the sensitivity to weak disorder potentials and variations in the carrier density could lead to signal noise and beam broadening effects. Even with ballistic mean free paths extending beyond the sample size, the beam may still follow irregular paths, as reported in III-V heterostructure 2D electron gas by Jura et al.⁷⁰. Second, it is pertinent to consider whether the state of the art of device fabrication can deliver the precision and reliability to make actual electron optics instruments feasible. While strain inhomogeneities and interfacial contamination present some of the more challenging issues for van der Waals heterostructure assembly³⁷, the field is developing rapidly. The key techniques for high quality van der Waals heterostructure assembly^{1,2,37,71}, edge contacts² and patterned layers^{37,72} were introduced and developed just a few years ago, and there is a significant effort in developing methods for scaling up the processes that presently rely on exfoliated materials. A suggestion for a possible fabrication scheme based on published techniques can be found in Supplementary Note 4.

Third, we consider the question regarding how quantum coherence will influence the operation of the microscope, beyond setting a limit for the image resolution in the tens of nanometer through diffraction effects. Coherence will for instance influence the angular distribution of electron beams passing through narrow apertures⁴⁷, leading to a broader beam according to the Huygens principle³⁴. This can, however, be countered by increasing of the aperture size and the carrier density to reduce the Fermi wavelength. Our semiclassical simulations indicate that the image formation is robust towards increasing the aperture size, as we show in Supplementary Fig. 6. As pointed out above, our simulations represent the mesoscopic limit, where electron currents are well approximated by classical trajectories/ray tracing^{35,56}. Upscaling of the lateral dimensions as a route to diminish

diffraction and coherence effects will benefit directly from continued development of sample quality^{2,12}. One exception is the scattering of Dirac fermion beams on small objects, where quantum coherence effects may cause significant deviations from the transmission signatures found from our semiclassical trajectory simulations. In Supplementary Note 3, we show maps of the atomistic bond current from atomistic tight binding calculations, for collimated Dirac fermion beams generated by parabolic lenses and narrow apertures. Three cases are presented, to illustrate the main concepts of this work: a caustic pattern corresponding to Fig. 5c, a triangular closed orbit in a circular pn-junction with jet currents corresponding to Fig. 5e, and scanning of a focused beam using the magnetic field across a small circular VD, as in Fig. 4 and Fig. 6. As expected, the simulations show that current density of structures which are large compared to the Fermi wavelength, show reasonable resemblance with the classical calculations, but also that quantum coherence leads to bond current patterns with a richer emission and reflection structure, which may be utilized to extract more detailed information of targets than possible with semiclassical calculations.

In that sense, we anticipate that quantum coherence is indeed an opportunity for developing more advanced functionality of the DFM. With phase-coherent beams, interferometric and even holographic microscopy could give new insight in conductance fluctuations and weak localization, since now individual or sets of trajectories can be selected without need for permanent wires, instead of ensemble averaged.

Along the same lines, we envision utilizing spin and valley degrees of freedom of graphene's charge carriers. For example, the long spin-life times in graphene^{73,74} may enable the use of spin-polarized electron beams to study magnetic edge terminations, magnetic molecules, or local proximity-induced spin-orbit interaction. For this ferromagnetic contacts can provide for spin-polarized injection and detection. A step further one could also imagine to make use of point contact-based spin and valley filters⁷⁵ for increasing the functionality of the DFM. An interesting

target for a spin polarized DFM would be strained nanobubbles⁷⁶ that exhibit huge pseudomagnetic fields and can act as spin filters and beam splitters⁷⁷. Focused beams could possibly also be used to investigate interactions between layers in more complex, multilayered heterostructures⁷². While the image resolution of a DFM can never rival those of established electron or scanning probe microscopies, the Dirac fermion microscope could provide new insight in the details of microscopic scattering processes⁶⁸ and interactions with the environment, disorder, adsorbed molecules, quantum dots, which are crucial for sensing, electronics and optoelectronics applications.

In a broader perspective, the Dirac fermion microscope embodies a wireless electron transport measurement system, where carriers can be injected, directed and focused onto objects of interest to perform a form of transport measurements without edge scattering, inflexibility and limitations of a permanent, hardwired physical wires.

Methods

The Monte Carlo simulations use a variable time step Verlet numerical integration algorithm, with optional disorder, and possibility of mixing numerical potential energy maps with coordinate-based, analytical geometrical boundaries to generate complex scattering landscapes. The target objects in Fig. 3 and Fig. 5b are modelled as nearly hard-walled potentials obtained by convoluting a step potential with a Gaussian function of less than 10 nm. In the simulation, the point contacts emit trajectories with uniform angular distribution (corresponding to a metallic contact), however, to optimize the calculation speed in certain configurations the distribution is artificially narrowed before passage through an aperture, see e.g. Fig. 5d. This only affects the computation time, as less time is spent on trajectories that will anyway hit the absorptive walls of the aperture enclosure. The transmissions between the electrodes are calculated by dividing the number of exiting trajectories

with the number of emitted trajectories; we do not take into account the variations in ballistic contact resistance for the different electron gun configurations, as the relative change in transmission with position or magnetic field is sufficient for image generation. The pn-junctions are modelled using the Cayssol approximation formula⁵⁸ with width $w = 10$ nm, unless stated otherwise, with the carrier density kept fixed at 10^{12} cm⁻², for both p and n -doped regions; these are typical values for electrostatically gated graphene. While the simulation was carried out in $4 \mu\text{m} \times 2 \mu\text{m}$ or $4.5 \mu\text{m} \times 1 \mu\text{m}$ area in all simulations, the dimensions of our proposed devices can immediately be scaled up. Increasing all dimensions by a factor of S will yield identical results by corresponding scaling of the cyclotron radius, i.e. by changing the magnetic field or the carrier density by a factor of S^{-1} or $S^{1/2}$, respectively. In a practical device, scaling the system up will reduce issues with diffraction i.e. through narrow apertures⁴⁷, but makes higher demands with respect to the mean free path and presence of small angle scattering effects⁷⁰; for fabrication of a real device, this is an important trade-off, and a strong motivation to push device quality in a similar manner as for III-V 2D electron systems⁶⁹. Atomistic tight binding calculations were performed to examine the scattering of focused, collimated dirac fermion beams on circular pn-junctions and provide a basis for comparison with the semiclassical calculations. The methodology and results of these calculations are described in Supplementary Note 3 and Supplementary Fig. 4.

Data Availability

All relevant data as well as the computer code for the semiclassical Monte Carlo simulations are available from the authors.

Acknowledgements

This work was supported by the Danish National Research Foundation (DNRF) Center for Nanostructured Graphene (DNRF103), the EU Graphene Flagship (604391), and DFF-EDGE (4184-00030). We are thankful for discussions with and suggestions from Peter Uhd-Jepsen, Antti-Pekka Jauho, Bjarke Sørensen Jessen, Lene Gammelgaard and Timothy J. Booth.

Author contributions

P. B. conceived the Dirac fermion microscope concept and carried out the semiclassical calculations, with significant contributions from the coauthors. G. C. performed the quantum transport calculations with M. B. and N. P. The manuscript was written by P. B. with assistance from the coauthors. J. C. contributed the caustic analysis. All authors discussed the results and commented on the manuscript.

Competing financial interests.

There are no competing financial interests among the authors.

References

- 1 Dean, C. R. *et al.* Boron nitride substrates for high-quality graphene electronics. *Nature Nanotechnology* **5**, 722-726 (2010).
- 2 Wang, L. *et al.* One-Dimensional Electrical Contact to a Two-Dimensional Material. *Science* **342**, 614-617 (2013).
- 3 Mayorov, A. S. *et al.* Micrometer-Scale Ballistic Transport in Encapsulated Graphene at Room Temperature. *Nano Letters* **11**, 2396-2399 (2011).
- 4 Moser, J., Barreiro, A. & Bachtold, A. Current-induced cleaning of graphene. *Applied Physics Letters* **91**, 163513 (2007).
- 5 Bolotin, K. I. *et al.* Ultrahigh electron mobility in suspended graphene. *Solid State Communications* **146**, 351-355 (2008).
- 6 Rickhaus, P. *et al.* Snake trajectories in ultraclean graphene p-n junctions. *Nature Communications* **6**, 6470 (2015).
- 7 Maurand, R. *et al.* Fabrication of ballistic suspended graphene with local-gating. *Carbon* **79**, 486-492 (2014).

- 8 Kaasbjerg, K., Thygesen, K. S. & Jacobsen, K. W. Unraveling the acoustic electron-phonon interaction in graphene. *Physical Review B* **85**, 165440 (2012).
- 9 Zhang, Y. B., Tan, Y. W., Stormer, H. L. & Kim, P. Experimental observation of the quantum Hall effect and Berry's phase in graphene. *Nature* **438**, 201-204 (2005).
- 10 Bandurin, D. A. *et al.* Negative local resistance caused by viscous electron backflow in graphene. *Science* **351**, 1055-1058 (2016).
- 11 Torre, I., Tomadin, A., Geim, A. K. & Polini, M. Nonlocal transport and the hydrodynamic shear viscosity in graphene. *Physical Review B* **92**, 165433 (2015).
- 12 Banszerus, L. *et al.* Ballistic Transport Exceeding 28 μm in CVD Grown Graphene. *Nano Letters* **16**, 1387-1391 (2016).
- 13 Young, A. F. & Kim, P. Quantum interference and Klein tunnelling in graphene heterojunctions. *Nature Physics* **5**, 222-226 (2009).
- 14 Baringhaus, J. *et al.* Exceptional ballistic transport in epitaxial graphene nanoribbons. *Nature* **506**, 349-354 (2014).
- 15 Novoselov, K. S. *et al.* Unconventional quantum Hall effect and Berry's phase of 2π in bilayer graphene. *Nature Physics* **2**, 177-180 (2006).
- 16 Bolotin, K. I., Ghahari, F., Shulman, M. D., Stormer, H. L. & Kim, P. Observation of the fractional quantum Hall effect in graphene. *Nature* **462**, 196-199 (2009).
- 17 Morozov, S. V. *et al.* Strong suppression of weak localization in graphene. *Physical Review Letters* **97**, 016801 (2006).
- 18 Tikhonenko, F. V., Horsell, D. W., Gorbachev, R. V. & Savchenko, A. K. Weak localization in graphene flakes. *Phys Rev Lett* **100**, 056802 (2008).
- 19 Sandner, A. *et al.* Ballistic Transport in Graphene Antidot Lattices. *Nano Letters* **15**, 8402-8406 (2015).
- 20 Dean, C. R. *et al.* Hofstadter's butterfly and the fractal quantum Hall effect in moire superlattices. *Nature* **497**, 598-602 (2013).
- 21 Ponomarenko, L. A. *et al.* Cloning of Dirac fermions in graphene superlattices. *Nature* **497**, 594-597 (2013).
- 22 Berger, C. *et al.* Electronic confinement and coherence in patterned epitaxial graphene. *Science* **312**, 1191-1196 (2006).
- 23 Rycerz, A., Tworzydło, J. & Beenakker, C. W. J. Anomalously large conductance fluctuations in weakly disordered graphene. *Epl* **79**, 57003 (2007).
- 24 Russo, S. *et al.* Observation of Aharonov-Bohm conductance oscillations in a graphene ring. *Physical Review B* **77**, 085413 (2008).
- 25 Huefner, M. *et al.* The Aharonov-Bohm effect in a side-gated graphene ring. *New Journal of Physics* **12**, 043054 (2010).
- 26 Taychatanapat, T., Watanabe, K., Taniguchi, T. & Jarillo-Herrero, P. Electrically tunable transverse magnetic focusing in graphene. *Nature Physics* **9**, 225-229 (2013).
- 27 Stander, N., Huard, B. & Goldhaber-Gordon, D. Evidence for Klein Tunneling in Graphene p-n Junctions. *Physical Review Letters* **102**, 026807 (2009).
- 28 Terres, B. *et al.* Size quantization of Dirac fermions in graphene constrictions. *Nature Communications* **7**, 11528 (2016).
- 29 Tombros, N. *et al.* Quantized conductance of a suspended graphene nanoconstriction. *Nature Physics* **7**, 697-700 (2011).
- 30 Castro Neto, A. H., Guinea, F., Peres, N. M. R., Novoselov, K. S. & Geim, A. K. The electronic properties of graphene. *Reviews of Modern Physics* **81**, 109-162 (2009).
- 31 Katsnelson, M. I., Novoselov, K. S. & Geim, A. K. Chiral tunnelling and the Klein paradox in graphene. *Nature Physics* **2**, 620-625 (2006).

- 32 Cheianov, V. V., Fal'ko, V. & Altshuler, B. L. The focusing of electron flow and a Veselago lens in graphene p-n junctions. *Science* **315**, 1252-1255 (2007).
- 33 Veselago, V. G. Properties of materials having simultaneously negative values of dielectric and magnetic susceptibilities. *Soviet Physics Solid State, USSR* **8**, 2854 (1967).
- 34 Lee, G. H., Park, G. H. & Lee, H. J. Observation of negative refraction of Dirac fermions in graphene. *Nature Physics* **11**, 925-929 (2015).
- 35 Chen, S. *et al.* Electron optics with p-n junctions in ballistic graphene. *Science* **353**, 1522-1525 (2016).
- 36 Rozhkov, A. V., Sboychakov, A. O., Rakhmanov, A. L. & Nori, F. Electronic properties of graphene-based bilayer systems. *Physics Reports-Review Section of Physics Letters* **648**, 1-104 (2016).
- 37 Pizzocchero, F. *et al.* The hot pick-up technique for batch assembly of van der Waals heterostructures. *Nature Communications* **7**, 11894 (2016).
- 38 Schwierz, F. Graphene transistors. *Nature Nanotechnology* **5**, 487-496 (2010).
- 39 Wilmart, Q. *et al.* A Klein-tunneling transistor with ballistic graphene. *2D Materials* **1**, 011006 (2014).
- 40 Bonaccorso, F., Sun, Z., Hasan, T. & Ferrari, A. C. Graphene photonics and optoelectronics. *Nature Photonics* **4**, 611-622 (2010).
- 41 Woessner, A. *et al.* Highly confined low-loss plasmons in graphene-boron nitride heterostructures. *Nature Materials* **14**, 421-425 (2015).
- 42 Levitov, L. & Falkovich, G. Electron viscosity, current vortices and negative nonlocal resistance in graphene. *Nature Physics* **12**, 672-676 (2016).
- 43 Sharma, P., Bernard, L. S., Bazigos, A., Magrez, A. & Ionescu, A. M. Room-Temperature Negative Differential Resistance in Graphene Field Effect Transistors: Experiments and Theory. *Acs Nano* **9**, 620-625 (2015).
- 44 Bhandari, S. *et al.* Imaging Cyclotron Orbits of Electrons in Graphene. *Nano Letters* **16**, 1690-1694 (2016).
- 45 Taychatanapat, T. *et al.* Conductance oscillations induced by ballistic snake states in a graphene heterojunction. *Nature Communications* **6**, 6093 (2015).
- 46 Lee, M. *et al.* Ballistic miniband conduction in a graphene superlattice. *Science* **353**, 1526-1529 (2016).
- 47 Barnard, A. W. *et al.* Absorptive pinhole collimators for ballistic Dirac fermions in graphene. *Preprint at <https://arxiv.org/abs/1611.05155>* (2016).
- 48 Liu, M. H., Gorini, C. & Richter, K. Creating and Steering Highly Directional Electron Beams in Graphene. *Physical Review Letters* **118**, 066801 (2017).
- 49 Molenkamp, L. W. *et al.* Electron-beam collimation with a quantum point contact. *Physical Review B* **41**, 1274-1277 (1990).
- 50 Tang, Y. *et al.* Flat-Lens Focusing of Electron Beams in Graphene. *Scientific Reports* **6**, 33522 (2016).
- 51 Park, C. H., Son, Y. W., Yang, L., Cohen, M. L. & Louie, S. G. Electron beam supercollimation in graphene superlattices. *Nano Letters* **8**, 2920-2924 (2008).
- 52 Williams, J. R., Low, T., Lundstrom, M. S. & Marcus, C. M. Gate-controlled guiding of electrons in graphene. *Nature Nanotechnology* **6**, 222-225 (2011).
- 53 LaGasse, S. W. & Lee, J. U. Understanding magnetic focusing in graphene p-n junctions through quantum modeling. *Preprint at <https://arxiv.org/abs/1612.05657>* (2016).
- 54 Rakyta, P., Kormanyos, A., Cserti, J. & Koskinen, P. Exploring the graphene edges with coherent electron focusing. *Physical Review B* **81**, 115411 (2010).

- 55 Van Houten, H. *et al.* Coherent electron focusing with quantum point contacts in a two-dimensional electron-gas. *Physical Review B* **39**, 8556-8575 (1989).
- 56 Milovanovic, S. P., Masir, M. R. & Peeters, F. M. Spectroscopy of snake states using a graphene Hall bar. *Applied Physics Letters* **103**, 233502 (2013).
- 57 Allain, P. E. & Fuchs, J. N. Klein tunneling in graphene: optics with massless electrons. *European Physical Journal B* **83**, 301-317 (2011).
- 58 Cayssol, J., Huard, B. & Goldhaber-Gordon, D. Contact resistance and shot noise in graphene transistors. *Physical Review B* **79**, 075428 (2009).
- 59 Rickhaus, P., Makk, P., Liu, M. H., Richter, K. & Schonenberger, C. Gate tuneable beamsplitter in ballistic graphene. *Applied Physics Letters* **107**, 251901 (2015).
- 60 Caridad, J. M., Connaughton, S., Ott, C., Weber, H. B. & Krstic, V. An electrical analogy to Mie scattering. *Nature Communications* **7**, 12894 (2016).
- 61 Gutierrez, C., Brown, L., Kim, C. J., Park, J. & Pasupathy, A. N. Klein tunnelling and electron trapping in nanometre-scale graphene quantum dots. *Nature Physics* **12**, 1069–1075 (2016).
- 62 McCloskey, D., Ballantine, K. E., Eastham, P. R. & Donegan, J. F. Photonic nanojets in Fresnel zone scattering from non-spherical dielectric particles. *Optics Express* **23**, 26326-26335 (2015).
- 63 Miao, F. *et al.* Phase-coherent transport in graphene quantum billiards. *Science* **317**, 1530-1533 (2007).
- 64 Rickhaus, P. *et al.* Ballistic interferences in suspended graphene. *Nature Communications* **4**, 2342 (2013).
- 65 Blaschke, J. & Brack, M. Periodic orbit theory of a circular billiard in homogeneous magnetic fields. *Physical Review A* **56**, 182-194 (1997).
- 66 Weiss, D. *et al.* Quantized periodic orbits in large antidot arrays. *Physical Review Letters* **70**, 4118-4121 (1993).
- 67 Boggild, P., Kristensen, A., Bruus, H., Reimann, S. M. & Lindelof, P. E. Periodic magnetoconductance fluctuations in triangular quantum dots in the absence of selective probing. *Physical Review B* **57**, 15408-15415 (1998).
- 68 Guinea, F. Models of Electron Transport in Single Layer Graphene. *Journal of Low Temperature Physics* **153**, 359-373 (2008).
- 69 Umansky, V., dePicciotto, R. & Heiblum, M. Extremely high-mobility two dimensional electron gas: Evaluation of scattering mechanisms. *Applied Physics Letters* **71**, 683-685 (1997).
- 70 Jura, M. P. *et al.* Unexpected features of branched flow through high-mobility two-dimensional electron gases. *Nature Physics* **3**, 841-845 (2007).
- 71 Haigh, S. J. *et al.* Cross-sectional imaging of individual layers and buried interfaces of graphene-based heterostructures and superlattices. *Nature Materials* **11**, 764-767 (2012).
- 72 Gorbachev, R. V. *et al.* Strong Coulomb drag and broken symmetry in double-layer graphene. *Nature Physics* **8**, 896-901 (2012).
- 73 Ingla-Aynes, J., Guimaraes, M. H. D., Meijerink, R. J., Zomer, P. J. & van Wees, B. J. 24- μm spin relaxation length in boron nitride encapsulated bilayer graphene. *Physical Review B* **92**, 2342 (2015).
- 74 Drogeler, M. *et al.* Spin Lifetimes Exceeding 12 ns in Graphene Nonlocal Spin Valve Devices. *Nano Letters* **16**, 3533-3539 (2016).
- 75 Rycerz, A., Tworzydło, J. & Beenakker, C. W. J. Valley filter and valley valve in graphene. *Nature Physics* **3**, 172-175 (2007).

- 76 Levy, N. *et al.* Strain-Induced Pseudo-Magnetic Fields Greater Than 300 Tesla in Graphene Nanobubbles. *Science* **329**, 544-547 (2010).
- 77 Settnes, M., Power, S. R., Brandbyge, M. & Jauho, A. P. Graphene Nanobubbles as Valley Filters and Beam Splitters. *Physical Review Letters* **117**, 276801 (2016).

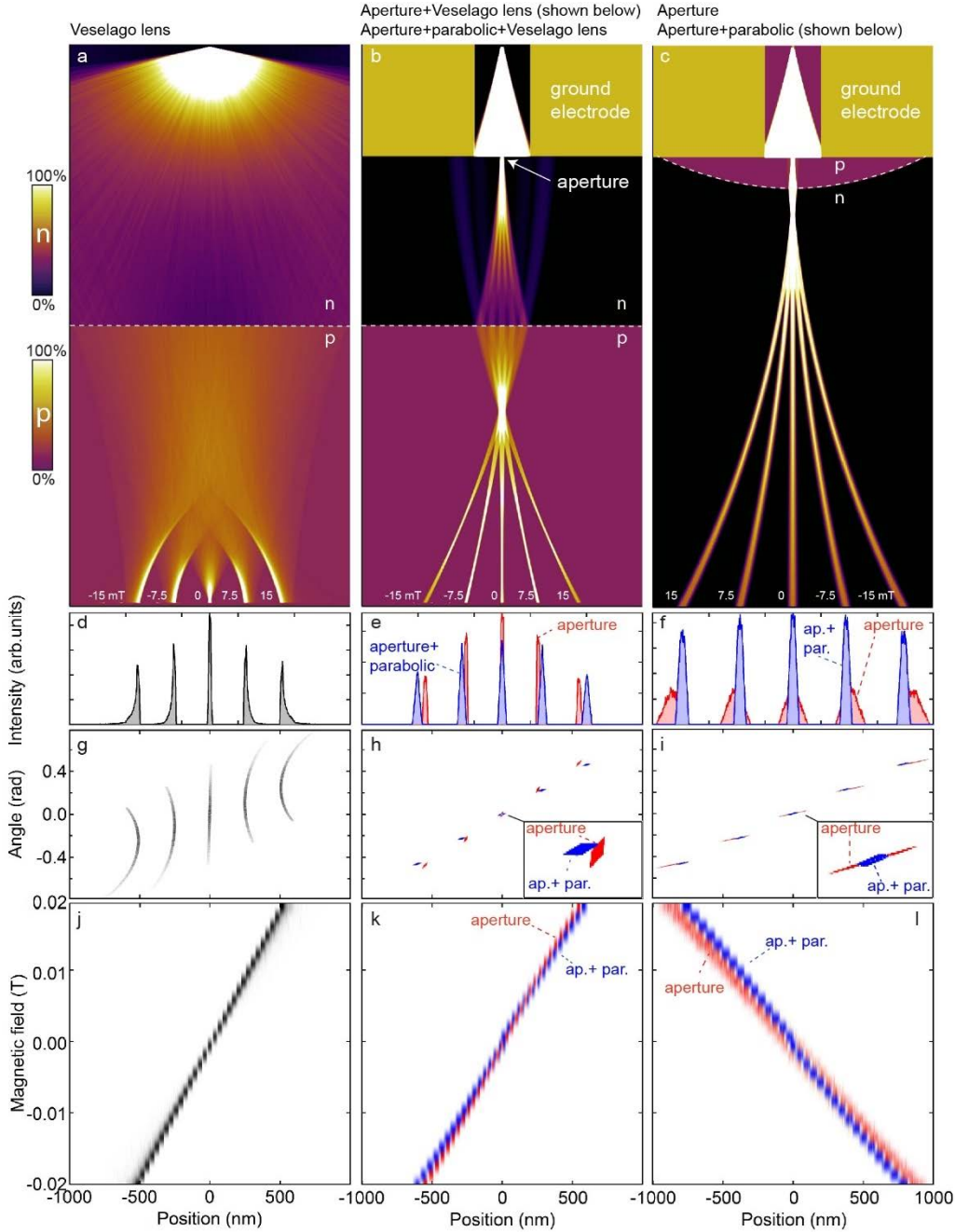
Supplementary Note 1 – Beam characteristics for 3 different microscope configurations.

In SI Fig. 1a-c, the three DFM configurations from Fig 3 in the main text are compared. The panel (a) shows the current density for configuration a conventional Veselago lens arrangement for five different magnetic fields (0 , ± 7.5 mT and ± 15 mT). Despite the wide injection distribution from the injection contact, the Veselago lensing results in strong caustics at the backplane electrode (which is also the focal plane), even at non-zero magnetic fields. The beam profile in (d), however, is increasingly asymmetric and distorted at high magnetic fields. The angular spread for trajectories exiting at the back electrode is nearly 1 radian for all B-fields, see panel (g). Clearly, even without collimative filtering, the Veselago lens can create a narrow, focused beam of electrons, with some broadening at non-zero magnetic fields, but also with very short focal depth. Despite the asymmetric beam profile, the position of the maximal beam intensity is nearly perfectly linear in magnetic field, see panel (j).

In SI Fig. 1b and 1c, an aperture is used to limit the beam divergence. In (b) a Veselago lens halfway from the source to the backplane, focus the beam, while in (c) there is none. For both (b) and (c), configurations with and without parabolic lenses were investigated, marked in panel (d-l) as red curves (aperture), and blue curves (aperture + parabolic lens).

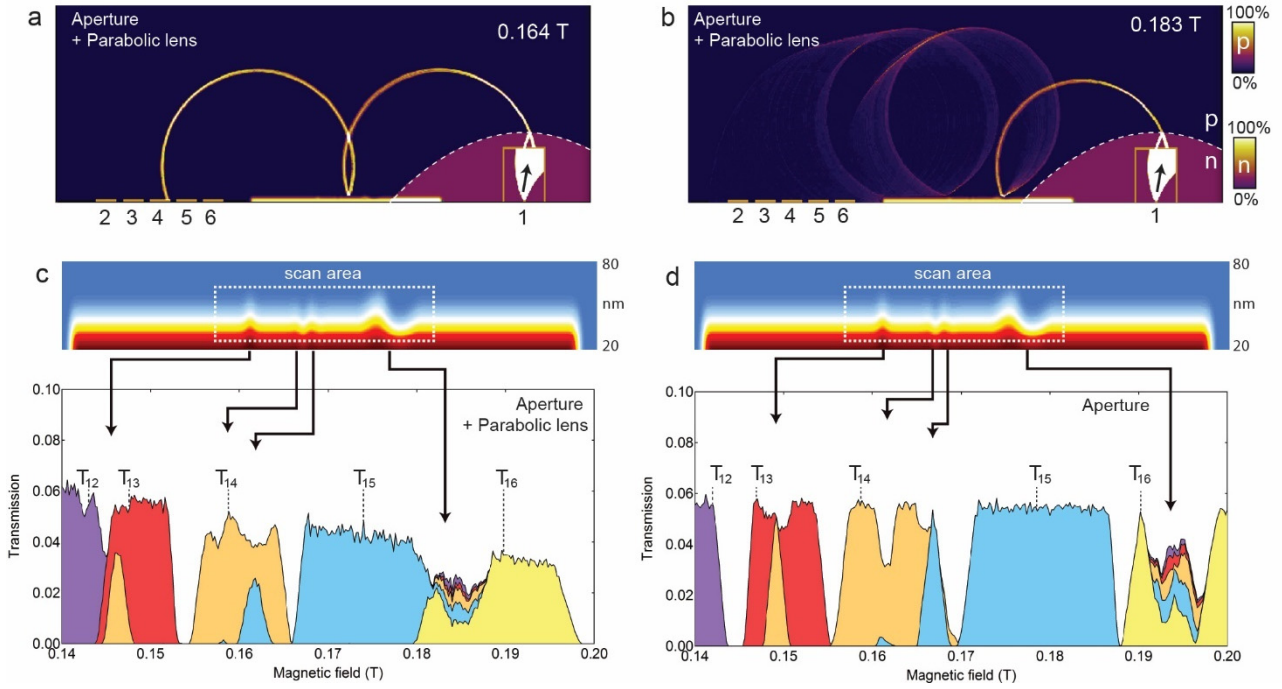
Panels (d-f) show the distribution of exit positions, which gives an indication of the beam shape and diameter. Panels (g-i) show the exit angle as a function of position. Panels (j-h) show the beam position as well as the beam diameter, as a function of magnetic field, however, with the axes switched to be compatible with the other panels, and shows how linearly the position depends on magnetic field.

The results differ slightly, with the sharpest beams obtained for configuration (b) without parabolic lens and configuration (c) with a parabolic lens, as in (b) the parabolic lens interferes with the focusing effect of the Veselago lens. Overall, the parabolic lens provides instead of strong focusing, a parallel, collimated beam. For configuration (c) the divergence is strongly reduced, see panel (f) and (i). In configuration (b), a small spread in angle (red) is changed to a spread in position (blue), see panel h and inset in panel (h). Both configuration (b) and (c) are close to having a linear dependence between magnetic field and position.



Supplementary Figure 1. Beam characteristics for 5 different microscope configurations.

Trajectory current density, and beam profile, angular distribution and position linearity as a function of magnetic field for the five configurations: Veselago (a), Aperture/Veselago (b), Aperture/Parabolic lens/Veselago (not shown), Aperture (not shown), Aperture/Parabolic (c). (d-f) Distribution of exit positions at back electrode. In (e) and (f) angular distributions for aperture without (blue) and with (red) a parabolic pn-junction after the aperture are shown. (g-i) Angle vs position of exiting trajectories at back electrode. (j-l) Position vs angle for different configurations with (blue) and without (red) a parabolic lens as a function of magnetic field.



Supplementary Figure 2. Imaging roughness of edges by multiterminal magnetic focusing. An array of 5 collector electrodes can give information on the local specularity of a scattering edge. (a) and (b) show a configuration with an aperture and a parabolic lens, where the beam is scanning across a surface with roughness variations of up to 20 nm in amplitude. The magnetic focusing trajectories are seen to be nearly free from divergence in this semiclassical limit. (c) Image of edge roughness where the envelope of the curves is the total (accumulated) transmission, $T_{\text{tot}} = T_{12} + T_{13} + T_{14} + T_{15} + T_{16}$, and the individual contributions are shown as different colors indicated on the graphs. Local edge roughness show up as increased transmission to neighbouring detectors, while specular scattering leads to only one transmission coefficient being non-zero at a time. The largest mixing of transmission currents occurs when the magnetic focusing beam pass by the largest protrusion, which is located at around 0.183 T) for the aperture/parabolic lens configuration and at around 0.195 T for the aperture configuration without the parabolic lens. The current is more constant and the features more distinct for the gun without parabolic lens. In SI Movie 4, the current density map evolution for configuration (b) is shown for apertures 25 nm and 50 nm. (d) Image of edge roughness, using an aperture without a parabolic lens. While the image is qualitatively similar to (c) the total (accumulated) transmission is more constant, with a larger impact on the transmission values ($B = 0.195$ T), compared to (b).

Supplementary Note 2. Caustics in circular scatterers

Circular potential barriers of different sizes in graphene are well-studied scattering objects in literature not only analytically but also experimentally. On one side, depending on the ratio between their radius and Fermi wavelength, they exhibit a diverse range of exotic transport phenomena, such as resonant scattering, quasi-bound states, caustics, rainbow and critical scattering effects¹⁻⁵. In addition, as a first approximation circular dots and voids have been used to model scattering in graphene caused by impurities, point defects, or metallic clusters placed on the graphene sheet⁶⁻¹⁰.

As explained in the main text, the semiclassical Monte Carlo simulations operates in the electron-optics regime, where the size of the scatterers is large in comparison with the Fermi wavelength¹. Therefore, the evaluation of our simulations will be based on circular potentials with large size ratio, $\lambda_F \ll R$. In particular, we perform direct comparisons between electron motion simulations obtained from our simulation and analytical approximations calculated in this optical regime for the electron motion inside circular potentials^{1-3,6,8}.

By considering the elastic scattering on plane electron waves in the low energy approximation, Cserti et al¹ show how the intensity maximum in graphene wavefunctions inside circular potentials form caustics which can be interpreted in the framework of geometrical optics using a negative refractive index, $n = -(k_{in} / k_{out}) = \sin \alpha / \sin \beta$ where k_{in} and k_{out} are the wavevectors inside and outside the circular potential (positive values)¹ and α, β are the angle of incidence and refraction, respectively (see SI Fig. 3, Inset). Here we show how the maximum current density calculated via our simulation perfectly follows these caustics, too. By doing so we demonstrate how our developed simulator is able to reproduce the complex interference patterns existing in these circular potentials, thus, ultimately checking its validity in a practical case which has been well-examined theoretically^{1-3,6} and experimentally⁴.

The envelope of the family of curves classified by impact parameter $b = R \sin \alpha$, where $-R \leq b \leq R$ (R is the radius of the circular potential) results in a caustic for each number of chords p inside the circle (corresponding to $p-1$ internal reflections). The curves of the caustic of the p th cord are then

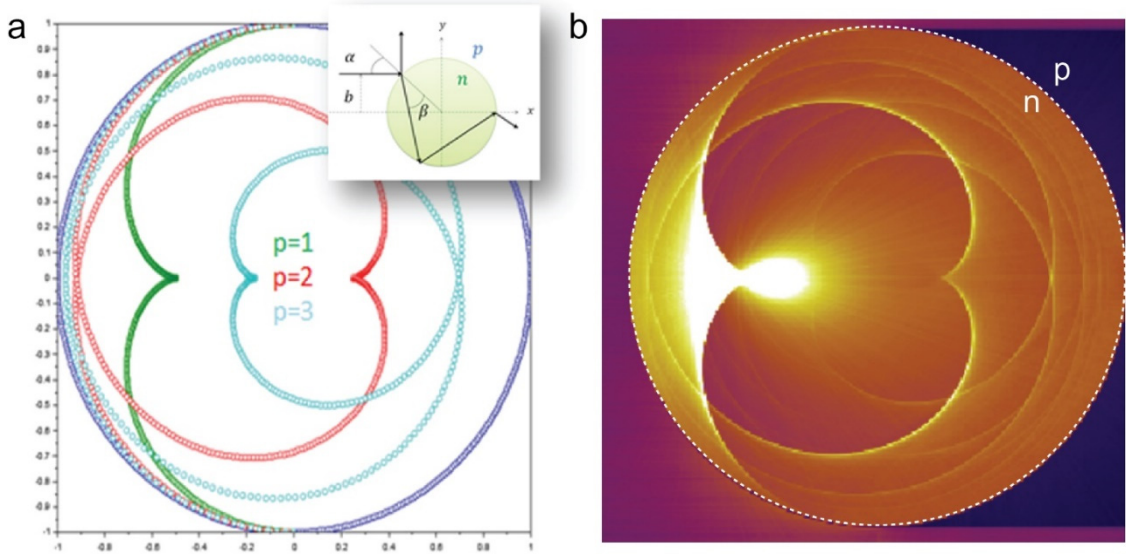
given in Cartesian coordinates $\begin{pmatrix} x_c(p, \alpha) \\ y_c(p, \alpha) \end{pmatrix}$, depending on the parameter $\alpha \left(-\frac{\pi}{2} \leq \alpha \leq \frac{\pi}{2} \right)$

by Ref¹:

$$\begin{pmatrix} x_c(p, \alpha) \\ y_c(p, \alpha) \end{pmatrix} = R(-1)^{p-1} \left[\begin{pmatrix} -\cos \theta \\ \sin \theta \end{pmatrix} + \cos \beta \frac{1+2(p-1)\beta'}{1+(2p-1)\beta'} \begin{pmatrix} \cos(\theta + \beta) \\ -\sin(\theta + \beta) \end{pmatrix} \right], \quad (1)$$

with $\theta(p, \alpha) = \alpha + 2(p-1)\beta$ and $\beta' = \frac{\cos \alpha}{\sqrt{n^2 - (\sin \alpha)^2}}$.

SI Figure 5 shows the corresponding caustics for the three first chords ($p=1,2,3$) for the case of $n = -1$, assuming $R = 1$. Along these caustics, the intensity maximum is located at a point called cusp which can be extracted by setting $\alpha = 0$ in Eq. 1. Importantly, it can be seen (SI Fig 3b) the formation of these caustics and cusps inside the circular dot is perfectly reflected in our montecarlo DMS when a circular scatterer is simultaneously impacted by a parallel beam of electrons, see Figure 5c, main text. We note how the caustics formed for larger chords $p > 3$, are less observable since in each internal reflection the intensity of the rays is decreased.



Supplementary Figure 3. Caustics inside circular scatterers due to negative refraction index. (a) Caustics formed for the three first chords, $p=1,2,3$ for an unit circle in the case of $n = -1$. Inset shows the ray path inside a circular pn-junction for an impact parameter b . (b) Current density calculated from Monte Carlo simulation with a parallel beam of electrons a symmetric, circular pn-junction with smoothness $w = 2.5$ nm. The maximum current densities perfectly follow the caustics from SI Eq. 1, in support of the usage of our simulations in the $\lambda_f \ll R$ regime.

Supplementary note 3. Atomistic quantum transport calculations.

We perform quantum transport simulations based on the non-equilibrium Green's function formalism within a nearest-neighbour tight-binding model, as implemented in the software package TBtrans¹¹. The SISL toolbox¹² has been used to set up a two-probe device Hamiltonian where a 2 nm wide zigzag graphene nanoribbon acts as a source contact at the edge of a 100 nm × 100 nm graphene flake (395.940 sites), with carbon-carbon bond length $a_0 = 0.142$ nm and hopping parameter $t_0 = 2.7$ eV. A drain electrode is placed on the graphene edge opposite of the source, while all other graphene edges are equipped with a complex absorbing potential¹³ to prevent artificial reflections. To ensure isotropic injection from the source we place an absorptive aperture¹⁴ with an opening of 1.5 nm at a distance of 3 nm from the ribbon/flake interface, which here plays the role of an isotropic point source. A symmetric p-n junction with a width of $w = 2$ nm is introduced by gradually modifying the on-site terms of the tight-binding. As in Liu et al.¹⁵, a parabolic junction with focal point located at the pinhole is used to collimate the electron beam from the source. A transverse magnetic field is accounted for using the Peierls substitution^{16,17}.

In order to study electron transport in our device we calculate bond-currents at $E = E_F$.

Instead of representing the individual bond current as a vector we plot the segment of length $a_0 / 2$ corresponding to the positive bond current only and with segment thickness and color scaled according to its magnitude. The same color range is used for all simulations, however, the maximum values have been adjusted for contrast. Areas with low to zero bond current appear white rather than dark, because the bond width is reduced to zero.

The area available for the quantum simulations is smaller than many of the structures considered in the main text. This can to some extent be dealt with by increasing the energy and using the scaling approximation valid for slowly varying potentials^{18,19}.

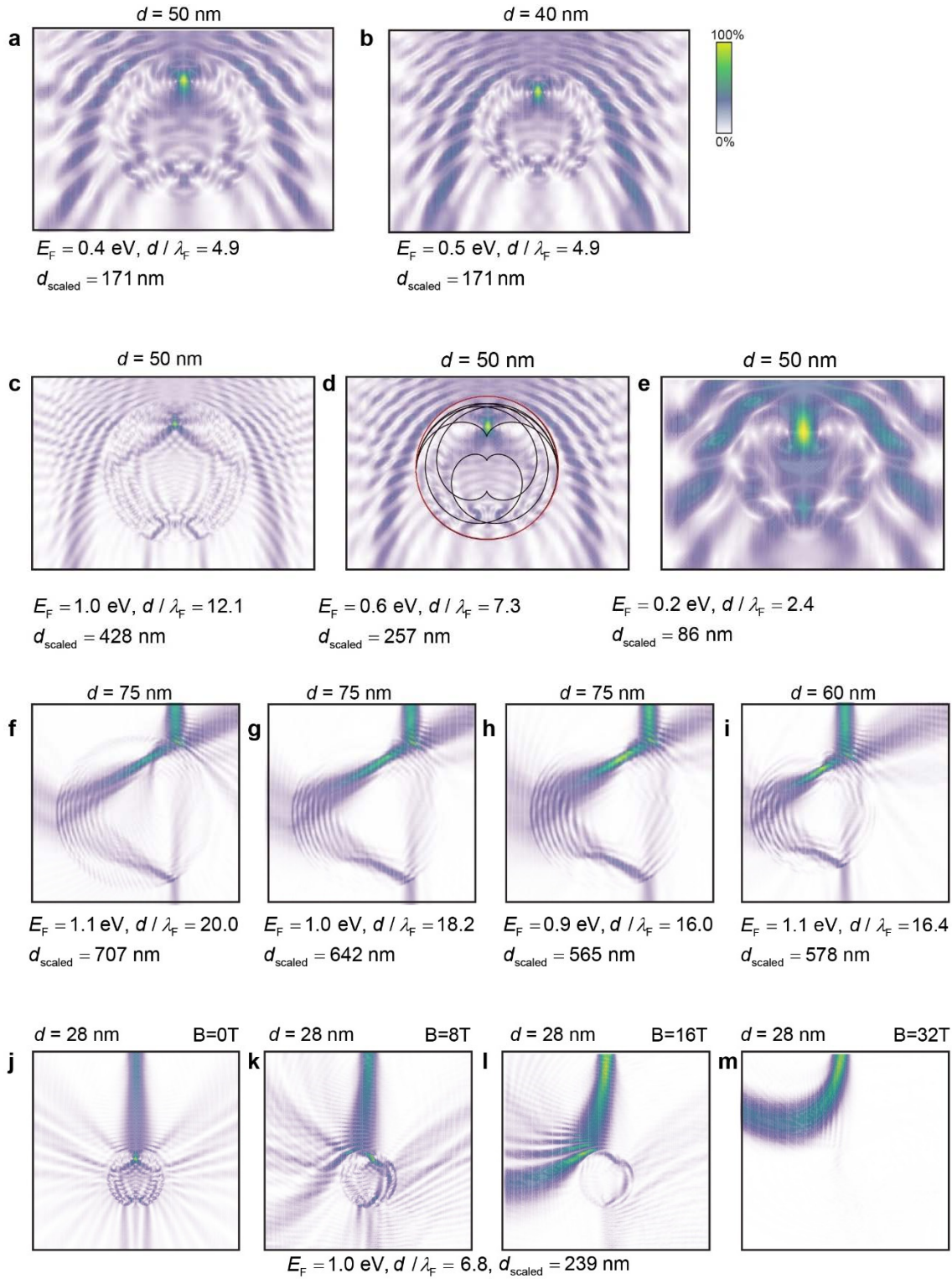
The bond current pattern for a small diameter d at a high energy, resembles the bond current pattern of a larger structure at low energy, provided they have similar ratio d / λ_F of diameter d and Fermi wavelength λ_F . For instance, the $d = 700$ nm diameter VD-potential as shown in Fig. 5(d) and Fig(e), will have $d \approx 20\lambda_F$ at $n = 10^{12} \text{ cm}^{-2}$, which corresponds to a 75 nm diameter VD

with $\lambda_F = 3.75$ nm and a Fermi energy of 1.1 eV. The 75 nm VD can be said to have a rescaled diameter of $d_{\text{scaled}} = 20 \times 35.4 \text{ nm} = 708 \text{ nm}$, i.e. equivalent diameter at $n = 10^{12} \text{ cm}^{-2}$.

SI Figure 4a and 4b show the caustic bond current patterns for two VD with (a) diameter $d=50$ nm and (b) $d=40$ nm, and $E = 0.4$ eV and 0.5 eV, respectively, both with $d / \lambda_F = 4.9$, corresponding to the rescaled diameter $d_{\text{scaled}} = 178 \text{ nm}$. As seen, the bond current patterns are virtually indistinguishable, which supports rescaling the calculations in this way, to compare with the semiclassical calculations in the main text.

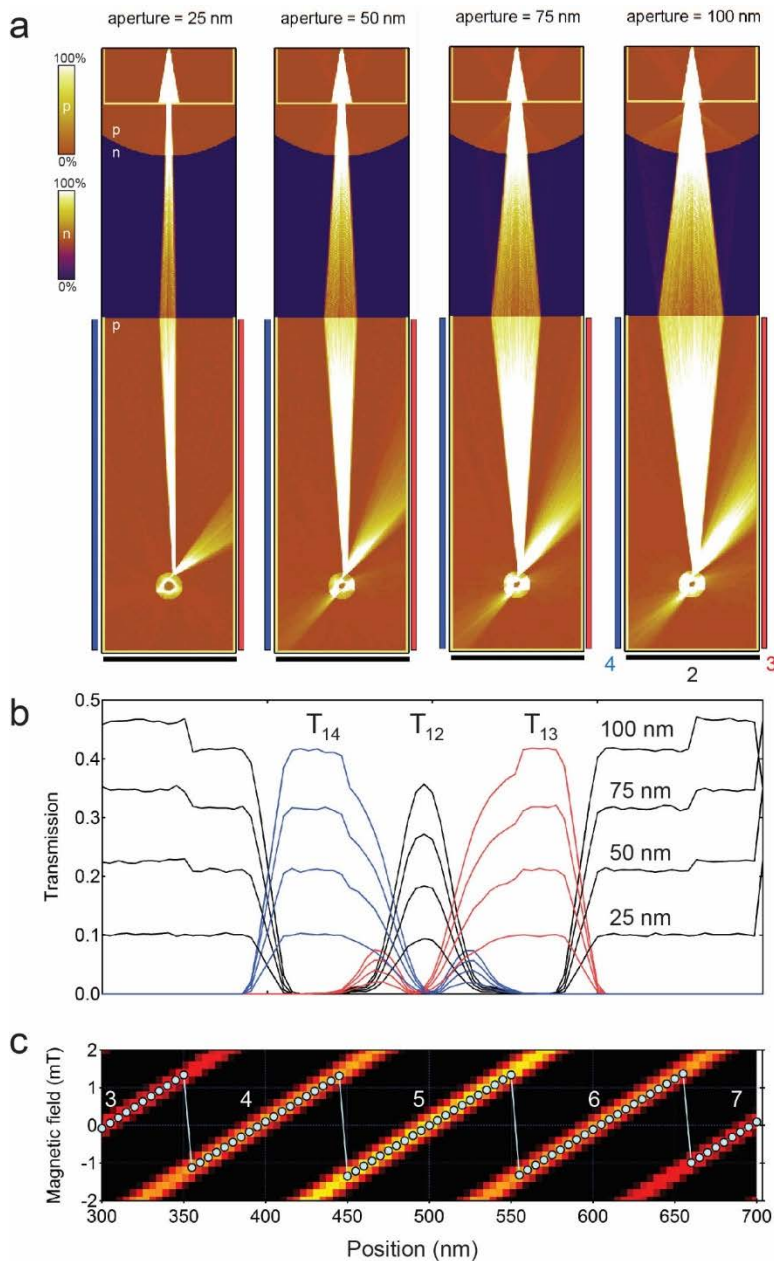
SI Figure 4c-e show the caustic patterns at different energy, 1.0, 0.6 and 0.2 eV, , which corresponds to the rescaled diameters $d_{\text{scaled}} = 428 \text{ nm}$, 257 nm and 86 nm , respectively. The caustic pattern from SI Fig. 3 superposed on SI Fig. 4d, are in reasonable agreement and very similar to the caustic patterns shown in Fig. 1 in Agrawal et al ²⁰.

SI Figure 4f-h shows a focused, collimated electron beam scattering on a 75 nm diameter circular pn-junction for different energies around 1 eV. The rescaled diameters d_{min} are in the range 707 nm to 578 nm. SI Figure 4i is 60 nm in diameter and an energy of $E_F = 0.9$ eV, which results in a $d_{\text{scaled}} = 578 \text{ nm}$. The d / λ_F ratio is nearly the same, 16.0 and 16.4, in the two cases, (h) and (i), and the bond current patterns are indeed very similar. The SI Fig. 4f has the same scaled diameter $d_{\text{scaled}} = 707 \text{ nm}$ as the VD simulated in Fig. 5e (main text), and similar current patterns both with respect to emission jets and the internal, triangularly shaped current structure. SI Fig. 4j-m show the bond currents for different magnetic fields, which are in rough qualitative agreement with Fig. 3 and Fig. 5 in the main text.



Supplementary Figure 4. Quantum transport calculations of DFM scattering from circular VD. (a-b) Comparison of bond current caustic pattern of two VD with different size and energy, but same $d / \lambda_F = 4.9$. (c-e) Bond current caustic patterns for a 50 nm VD with $E_F = 1.0 \text{ eV}$, 0.6 eV and 0.2 eV . These energies correspond to VDs with diameters $d_{\text{scaled}} = 428 \text{ nm}$,

257 nm and 86 nm for $n = 10^{12} \text{ cm}^{-2}$ ($E_F = 0.117 \text{ eV}$), used in the main text. The classical caustics from SI Fig. 3 are superposed on panel **(d)**. **(f-h)** A focused DF beam is impinging on a large circular VD with a diameter of 75 nm and energies $E_F = 1.1 \text{ eV}$, 1.0 eV and 0.9 eV . The bond current distribution for $E = 1.1 \text{ eV}$ ($d_{\text{scaled}} = 707 \text{ nm}$) is in agreement with the semiclassical current density of the 700 nm dot diameter in Fig 5h, main text. Comparison of **(h)** and **(i)** confirms that structures with similar $d / \lambda_F \approx 16$ have very similar bond current distribution. **(j-m)** Collimated DF beam scanning across a small VD ($d = 28 \text{ nm}$, $d_{\text{scaled}} = 239 \text{ nm}$) with an energy $E_F = 1.0 \text{ eV}$. The bond current scattering patterns roughly resemble the semiclassical simulations shown in Fig. 4, and Fig. 6, main text.

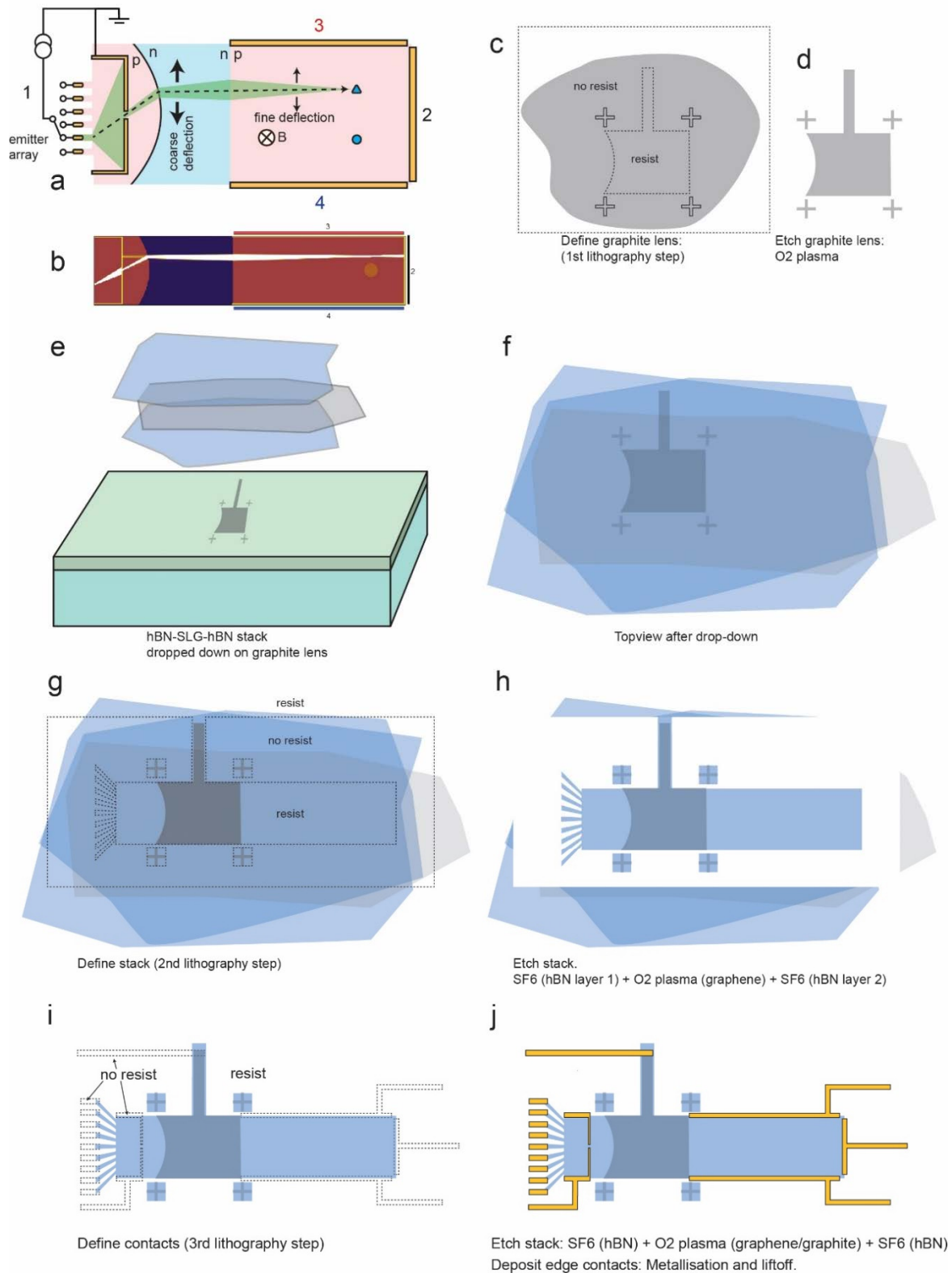


Supplementary Figure 5. DFM with increasing aperture. (a) Current density plots for the aperture being increased in steps of 25 nm from 25 nm to 100 nm, with a 200 nm diameter circular pn-junction (smoothness $w = 10$ nm) as the target. (b) The transmission images at the three electrodes 2, 3 and 4 are similar except for a scaling factor due to the higher currents passing through the larger aperture. The current stitching errors are increasing (i.e. at 350 nm and 660 nm) as the current calibration for the smallest aperture was used for all four curves. (c) The magnetic field and emitters are shown versus beam position to illustrate the stitching scheme, with the changes from emitter 3 through 7.

Supplementary Note 4. Suggested process flow for DFM.

We provide here one possible solution to fabricate the Dirac fermion microscope (DFM) configuration with the coaligned beam and multiple emitters, which is the most complex of our devices. The process flow is a suggestion for a starting point for fabricating the conceptual device, and will most likely require further adaption and optimization. The fabrication process is based on the hot-pickup van der Waals method, Pizzocchero et al, Nat. Comm (2016), Ref. ²¹.

SI Figure 6 shows in panel (a) an illustration of the DFM and (b) a Monte Carlo simulation of a $4.5\ \mu\text{m} \times 1\ \mu\text{m}$ DFM with 9 emitters. The 100 nm resolution requirement to define the emitter array as well as the narrow aperture can be demanding, so scaling the device by a factor of 5-10 (as discussed in the main text) will make it far easier to fabricate with standard electron beam lithography systems (typical : 30 keV), as well as reduce diffraction through the narrow aperture. SI Figure 6(c) illustrates a piece of few-layer graphite (below 10 layers) for the backgate that defines both the parabolic and the flat Veselago lens (see Fig. 5 in main text). SI Figure 6 (d) shows the graphite blockpatterned with a positive, high resolution resist (e.g PMMA, ZEP-520A or CSAR), and etched in an oxygen plasma. Four alignment marks are left to enable correct aligning of the subsequent lithography patterns (SI Fig. 6(e)). A large clean stack is prepared by self-cleaning (hot-pickup method) and dropped down on the graphite gate, shown in top view in SI Fig. 6(f). The bottom hBN should be around 10 nm or less, for the electron lenses to work optimally. SI Fig. 6(g) illustrates the second lithography step which defines the stack as well as the emitter leads. In SI Fig. 6(h) the resist is here used as an etch mask directly; alternatively, an Al etch mask can be used to achieve better etch resistance and definition of the finest structures. After etching of the three layers by a SF₆ etch (hBN), a brief oxygen plasms (graphene) followed by a second SF₆ etch (hBN) as described in Ref²¹, the device is ready for metal contacts. SI Fig. 6 (i) illustrates a third lithography step , followed by SF₆/O₂/SF₆ etch to open the stack for electrical contacts(SI Fig. 6 (j)), as well as to the graphite back gate. Cr/Au or Cr/Pd/Au contacts deposition and lift-off, concludes the process.



Supplementary Figure 6. Possible process flow to fabricate DFM devices. The process is based on the hot-pickup technique²¹ and previous methods mentioned herein, and is intended as a starting point. See SI Note 4, for description of the individual steps.

References

- 1 Cserti, J., Palyi, A. & Peterfalvi, C. Caustics due to a negative refractive index in circular graphene p-n junctions. *Physical Review Letters* **99**, 246801 (2007).
- 2 Heinisch, R. L., Bronold, F. X. & Fehske, H. Mie scattering analog in graphene: Lensing, particle confinement, and depletion of Klein tunneling. *Physical Review B* **87**, 155409 (2013).
- 3 Wu, J. S. & Fogler, M. M. Scattering of two-dimensional massless Dirac electrons by a circular potential barrier. *Physical Review B* **90**, 235402 (2014).
- 4 Caridad, J. M., Connaughton, S., Ott, C., Weber, H. B. & Krstic, V. An electrical analogy to Mie scattering. *Nature Communications* **7**, 12894 (2016).
- 5 Logemann, R., Reijnders, K. J. A., Tudorovskiy, T., Katsnelson, M. I. & Yuan, S. J. Modeling Klein tunneling and caustics of electron waves in graphene. *Physical Review B* **91**, 045420 (2015).
- 6 Katsnelson, M. I., Guinea, F. & Geim, A. K. Scattering of electrons in graphene by clusters of impurities. *Physical Review B* **79**, 195429 (2009).
- 7 McCreary, K. M. *et al.* Effect of cluster formation on graphene mobility. *Physical Review B* **81**, 115453 (2010).
- 8 Guinea, F. Models of Electron Transport in Single Layer Graphene. *Journal of Low Temperature Physics* **153**, 359-373 (2008).
- 9 Hentschel, M. & Guinea, F. Orthogonality catastrophe and Kondo effect in graphene. *Physical Review B* **76**, 115407 (2007).
- 10 Vaishnav, J. Y., Anderson, J. Q. & Walls, J. D. Intravalley multiple scattering of quasiparticles in graphene. *Physical Review B* **83**, 165437 (2011).
- 11 Papior, N., Lorente, N., Frederiksen, T., Garcia, A. & Brandbyge, M. Improvements on non-equilibrium and transport Green function techniques: The next-generation TRANSIESTA. *Computer Physics Communications* **212**, 8-24 (2017).
- 12 Nick R. Papior. sisl: v0.8.3. (2017). doi:10.5281/zenodo.495025
- 13 Xie, H., Kwok, Y., Jiang, F., Zheng, X. & Chen, G. H. Complex absorbing potential based Lorentzian fitting scheme and time dependent quantum transport. *Journal of Chemical Physics* **141**, 164122 (2014).
- 14 Barnard, A. W. *et al.* Absorptive pinhole collimators for ballistic Dirac fermions in graphene. Preprint at <https://arxiv.org/abs/1611.05155> (2016).
- 15 Liu, M.-H., Gorini, C. & Richter, K. Creating and Steering Highly Directional Electron Beams in Graphene. *Physical Review Letters* **118**, 066801 (2017).
- 16 Peierls, R. On the theory of diamagnetism of conduction electrons. *Zeitschrift Fur Physik* **80**, 763-791 (1933).
- 17 Pedersen, J. G. & Pedersen, T. G. Tight-binding study of the magneto-optical properties of gapped graphene. *Physical Review B* **84**, 115424 (2011).
- 18 Liu, M. H. *et al.* Scalable Tight-Binding Model for Graphene. *Physical Review Letters* **114**, 036601 (2015).
- 19 Beconcini, M. *et al.* Scaling approach to tight-binding transport in realistic graphene devices: The case of transverse magnetic focusing. *Physical Review B* **94**, 115441 (2016).
- 20 Agrawal, N., Ghosh, S. & Sharma, M. Scattering of massless Dirac fermions in circular p-n junctions with and without magnetic field. *Journal of Physics-Condensed Matter* **26**, 155301 (2014).

- 21 Pizzocchero, F. *et al.* The hot pick-up technique for batch assembly of van der Waals heterostructures. *Nature Communications* **7**, 11894 (2016).